Analysis of conditional colocalization relationships and hierarchies in three-color microscopy images

Running title: Conditional colocalization in 3-color images

Jesus Vega-Lugo[1,a], Bruno da Rocha-Azevedo[1,a], Aparajita Dasgupta[1], Nicolas Touret[2], Khuloud Jaqaman[1,3,b]

[1] Department of Biophysics, UT Southwestern Medical Center, Dallas, TX 75390, USA

[2] Department of Biochemistry, University of Alberta, Edmonton, Alberta, T6G 2H7, Canada

[3] Lyda Hill Department of Bioinformatics, UT Southwestern Medical Center, Dallas, TX 75390, USA

[a] Equal contribution

[b] Corresponding author: khuloud.jaqaman@utsouthwestern.edu

Abstract

Colocalization analysis of multicolor microscopy images is a cornerstone approach in cell biology. It provides information on the localization of molecules within various subcellular compartments and allows the interrogation of molecular interactions in their cellular context. However, almost all colocalization analyses are designed for two-color images. This limits their applicability and the type of information that they reveal, leading to underutilization of multicolor microscopy images. Here we describe an approach, termed "conditional colocalization analysis," for analyzing the colocalization relationships between three molecular entities in three-color microscopy images. Going beyond the question of whether colocalization is present or not, it addresses the question of whether the colocalization between two entities is influenced, positively or negatively, by their colocalization with a third entity. We showcase two applications of conditional colocalization analysis, one addressing the question of compartmentalization of molecular interactions, and one investigating the hierarchy of molecular interactions in a multimolecular complex. The software for conditional colocalization analysis is available at https://github.com/kjaqaman/conditionalColoc.

Introduction

Multimolecular interactions are the basis of cellular functions. High-resolution and super-resolution fluorescence microscopy allow us to routinely image three, four, or even more molecular entities at the same time within a cell (Huang et al., 2009; Sahl et al., 2017; Valm et al., 2017). Such multicolor imaging may provide a wealth of information about the spatiotemporal regulation of multimolecular interactions in their cellular context. However, without computational and quantitative analysis, much of this information remains unextracted (Bolte and Cordelières, 2006; Lagache et al., 2015).

Colocalization analysis is a cornerstone technique in cell biology for the analysis of multicolor microscopy images. It provides information on the localization of molecules within various subcellular compartments, shedding light on their function (Bolte and Cordelières, 2006; Dunn et al., 2011). For known molecular interactions, it allows their interrogation in their spatiotemporal cellular context, complementing biochemical and biophysical techniques, which detect interactions but taken out of their cellular context (Caetano et al., 2015; Helmuth et al., 2010; Lagache et al., 2018; Lagache et al., 2015). However, the overwhelming majority of colocalization analyses are applicable to only two-color microscopy images, i.e. they investigate only pairs of molecular entities. The few previous studies involving three-color colocalization were focused on either the question of whether the three imaged entities colocalize (Fletcher et al., 2010; Stauffer et al., 2018) or the question of mutually exclusive colocalization of one entity with the other two (Sastre et al., 2019). This greatly limits their applicability and the type of information that they may reveal, leading to underutilization of multicolor microscopy images.

Here we developed an approach for analyzing the colocalization relationships between three molecular entities, termed “conditional colocalization analysis,” based on spatial point pattern analysis of detected objects in microscopy images (Diggle, 2014; Helmuth et al., 2010; Lagache et al., 2015; Pastorek et al., 2016). Going beyond the question of whether colocalization is present or not, it addresses the question of whether the colocalization between two molecular entities is influenced, positively or negatively, by their colocalization with a third entity. For molecules known to interact (as identified via biochemical and/or biophysical techniques), the extracted colocalization relationships provide evidence for the cooperativity or competition between interactions, and for the enhancement or suppression of interactions at particular subcellular locations, domains or compartments.

To highlight the capabilities of conditional colocalization analysis, we applied it to two problems addressing different facets of molecular interactions and their regulation. In the first, we investigated the colocalization relationships between a receptor and its downstream effector in the context of functionally

relevant plasma membrane locations, shedding light on the spatial compartmentalization of these interactions. In the second, we investigated the hierarchy of molecular interactions between three proteins, as a first step toward understanding the network of molecular interactions in which these molecules are involved.

Results

Derivation of conditional colocalization measures

To derive measures that reflect the extent to which one molecular entity influences – positively or negatively – the colocalization between two other molecular entities, we took a spatial point pattern analysis approach (Diggle, 2014; Helmuth et al., 2010; Lagache et al., 2015; Pastorek et al., 2016). Specifically, objects (i.e. the labeled molecular entities) in the images were first detected or segmented, and then their colocalization was assessed based on their nearest neighbor distance. We took this approach for two main reasons. First, for a basic measure of the extent of colocalization between two object types, the nearest neighbor distance allowed us to calculate the fraction of one object type colocalized with another object type (Helmuth et al., 2010; Lachmanovich et al., 2003). By interpreting colocalization fractions as probabilities, we were able to extend the analysis to calculate conditional probabilities and similar measures that reflected the relationships between object colocalizations, thus allowing us to address the question of the influence of one molecular entity on the colocalization of two other molecular entities. Second, object-based analysis offered more robust means to computationally assess the significance of any observed colocalization than pixel-based analysis such as the Pearson correlation function, as it allowed for (computationally) abolishing the relationships between objects (e.g. by object randomization) while maintaining individual object integrity (Fletcher et al., 2010; Lagache et al., 2015).

Throughout this work, we will employ the following terminology to refer to the three object types the colocalization relationships of which are being analyzed. The objects will be referred to as target (T), reference (R) and condition (C). Using this terminology, the question that the analysis aims to answer is: *How much is the colocalization of target objects with reference objects influenced by target and/or reference colocalization (or not) with condition objects?* To answer this question, we employed a four-step analysis process. For simplicity, the below descriptions and derivations are for images containing diffraction-limited, punctate objects, the positions of which are described by their center coordinates (determined, with sub-pixel precision, by fitting the signal with a Gaussian that approximates the

microscope point spread function (Aguet et al., 2013; Jaqaman et al., 2008)). In the next section, we present an extension to the case when one channel contains non-punctate objects.

Step 1. Divide target and reference into groups colocalized or not colocalized with condition.

Suppose there are N_T, N_R and N_C target, reference and condition objects, respectively (**Figure 1A**). First, we determined for each target object and each reference object whether it colocalized with a condition object (**Figure 1A, B**). Those that colocalized with a condition object were in the condition-positive groups (TwC and RwC; "w" indicates "with"), while those that did not colocalize with any condition object were in the condition-negative groups (TnC and RnC; "n" indicates "without").

Two objects were considered colocalized when the distance between their centers was below a particular colocalization radius. The colocalization radius could be set differently for each pair of channels, to account for the objects' localization precision and the registration shift between each pair of channels. An important point to remember regarding localization precision is that, by definition, one detects the fluorophore labeling the object of interest, and not the object of interest itself. Thus, the true object localization precision will most likely be lower than the localization precision reflecting the signal-to-noise ratio (SNR) of the images (Bates et al., 2007).

This division yielded the probability (p) of target and reference objects to colocalize with condition objects:

$$p(TwC) = f_{coloc}(TwC) = N_{TwC}/N_T, \quad (1)$$

$$p(RwC) = f_{coloc}(RwC) = N_{RwC}/N_R, \quad (2)$$

where N_{TwC} and N_{RwC} are, respectively, the number of target objects and reference objects colocalized with condition objects. In **Eqs. 1, 2** (and all throughout this work), $p(\ldots)$ and $f_{coloc}(\ldots)$ indicate colocalization probability and colocalization fraction, respectively. These colocalization probabilities are equivalent to the colocalization measure proposed in (Helmuth et al., 2010) (where they are called "C^T").

Step 2. Calculate the fraction of target colocalizing with reference for the different group combinations.

Next, we calculated the fractions of target objects in the different groups colocalized with reference objects in the different groups, also using the colocalization algorithm of (Helmuth et al., 2010). As in Step 1, two objects were considered colocalized when the distance between their centers was below a particular colocalization radius. From this, we obtained five colocalization fractions: $f_{coloc}(TwR)$ (for all target and reference), $f_{coloc}\big((TwC)wR\big)$ (for the condition-positive group of target), $f_{coloc}\big((TnC)wR\big)$

(for the condition-negative group of target), $f_{coloc}\big(Tw(RwC)\big)$ (for the condition-positive group of reference), and $f_{coloc}\big(Tw(RnC)\big)$ (for the condition-negative group of reference).

For each colocalization fraction, we also calculated a corresponding coincidental colocalization fraction in the absence of any true relationship between target and reference (f_{coloc}^{nullTR}). For this, we kept the reference objects in place, and replaced the target objects with points on a grid within the cell area, as described in (Helmuth et al., 2010). Using the same colocalization radius as for the original data, we calculated f_{coloc}^{nullTR} corresponding to each of the colocalization fractions mentioned above. A strength of this procedure is that it calculates the expected colocalization given the number and spatial distribution of the reference objects, i.e. it considers the spatial context of the colocalization analysis (Helmuth et al., 2010).

Step 3. Calculate conditional colocalization measures from colocalization fractions.

The colocalization fractions obtained in Step 2 yielded the following conditional colocalization measures:

- **The overall colocalization probability ($\boldsymbol{p(TwR)}$):**

  The all target vs. all reference analysis (**Figure 1C**, top row) yielded the overall probability of target to colocalize with reference, regardless of either's relationship to condition:

$$p(TwR) = f_{coloc}(TwR) = N_{TwR}/N_T. \tag{3}$$

  N_{TwR} is the number of target objects colocalized with reference objects, irrespective of either's relationship to condition objects (**Figure 1C**, top row).

- **Influence of target colocalization with condition on target colocalization with reference ($\boldsymbol{p(TwR|TwC)}$ and $\boldsymbol{p(TwR|TnC)}$):**

  For this, the condition-positive target vs. all reference and condition-negative target vs. all reference analyses (**Figure 1D**) yielded:

$$f_{coloc}\big((TwC)wR\big) = N_{(TwC)wR}/N_{TwC}, \tag{4}$$

$$f_{coloc}\big((TnC)wR\big) = N_{(TnC)wR}/N_{TnC}. \tag{5}$$

  $N_{(TwC)wR}$ is the number of condition-positive target objects colocalized with reference objects (i.e. target objects colocalized with both reference objects and condition objects) (**Figure 1D**, left branch). $N_{(TnC)wR}$ is the number of condition-negative target objects colocalized with reference objects (i.e. target objects colocalized with reference objects but not with condition objects) (**Figure 1D**, right branch). N_{TwC} and N_{TnC} are the number of condition-positive and condition-negative target objects, respectively (from Step 1).

It follows from **Eqs. 4, 5** that $f_{coloc}\big((TwC)wR\big)$ and $f_{coloc}\big((TnC)wR\big)$ indicate the conditional probabilities of target to colocalize with reference given that target is, respectively, colocalized, or not colocalized, with condition:

$$p(TwR|TwC) = p(TwR\&TwC)/p(TwC) = \big(N_{(TwC)wR}/N_T\big)/(N_{TwC}/N_T)$$
$$= N_{(TwC)wR}/N_{TwC} = f_{coloc}\big((TwC)wR\big). \quad (6)$$

$$p(TwR|TnC) = p(TwR\&TnC)/p(TnC) = \big(N_{(TnC)wR}/N_T\big)/(N_{TnC}/N_T)$$
$$= N_{(TnC)wR}/N_{TnC} = f_{coloc}\big((TnC)wR\big). \quad (7)$$

These are useful measures for conditional colocalization analysis, as their comparison to each other and to $p(TwR)$ would answer the question whether the extent to which target colocalization with reference is influenced by target colocalization (or not) with condition.

- **Influence of reference colocalization with condition on target colocalization with reference ($\boldsymbol{p^{rs}\big(Tw(RwC)\big)}$ and $\boldsymbol{p^{rs}\big(Tw(RnC)\big)}$):**

For this, the all target vs. condition-positive reference and all target vs. condition-negative reference analyses (**Figure 1C**, bottom row) yielded:

$$p\big(Tw(RwC)\big) = f_{coloc}\big(Tw(RwC)\big) = N_{Tw(RwC)}/N_T, \quad (8)$$
$$p\big(Tw(RnC)\big) = f_{coloc}\big(Tw(RnC)\big) = N_{Tw(RnC)}/N_T. \quad (9)$$

$N_{Tw(RwC)}$ is the number of target objects colocalized with reference objects that are themselves colocalized with condition objects. $N_{Tw(RnC)}$ is the number of target objects colocalized with reference objects that are not colocalized with condition objects (**Figure 1C**, bottom row).

While this analysis yielded the probabilities of target to colocalize with the indicated subsets of reference objects, these probabilities were not useful as is for answering the question whether the extent of target colocalization with reference is influenced by reference colocalization (or not) with condition. The reason is that the number of reference objects used in the different analyses is different. As a result, $N_{RwC} + N_{RnC} = N_R$ (**Figure 1B**, bottom), $N_{Tw(RwC)} + N_{Tw(RnC)} = N_{TwR}$ (**Figure 1C**, bottom row), and $p\big(Tw(RwC)\big) + p\big(Tw(RnC)\big) = p(TwR)$ (**Eqs. 8, 9** vs. **Eq. 3**).

However, in the absence of any special relationship between target objects and condition-positive or condition-negative reference objects, $p\big(Tw(RwC)\big)$ is expected to be $p(TwR)$ multiplied by N_{RwC}/N_R ($= p(RwC)$; **Eq. 2**), while $p\big(Tw(RnC)\big)$ is expected to be $p(TwR)$ multiplied by N_{RnC}/N_R ($= p(RnC) = 1 - p(RwC)$). Thus, for a measure of the influence of reference colocalization with condition on the colocalization of target with reference, we rescaled the colocalization probabilities to factor out $p(RwC)$ and $p(RnC)$.

186 $$p^{rs}\big(Tw(RwC)\big) = p\big(Tw(RwC)\big)/p(RwC), \quad (10)$$

187 $$p^{rs}\big(Tw(RnC)\big) = p\big(Tw(RnC)\big)/\big(1 - p(RwC)\big). \quad (11)$$

188 Note that these measures could be > 1, and thus they no longer indicated probabilities (unlike the
189 original fractions in **Eqs. 8, 9**). Nevertheless, the rescaling factored out the number of reference
190 objects used for analysis, allowing us to compare $p^{rs}\big(Tw(RwC)\big)$ and $p^{rs}\big(Tw(RnC)\big)$ to $p(TwR)$,
191 thus making these rescaled probabilities useful measures for assessing the extent to which target
192 colocalization with reference is influenced by reference colocalization (or not) with condition.

193 In summary, **Eqs. 3, 6, 7, 10 and 11** provided us with useful measures for conditional colocalization
194 analysis, to answer the question whether the extent of target colocalization with reference is influenced
195 by either's colocalization with the condition. Using f_{coloc}^{nullTR} instead of f_{coloc} in these equations yielded the
196 coincidental counterparts of these measures in the absence of any true relationship between target and
197 reference (p_{nullTR} or p_{nullTR}^{rs}).

198

199 ***Step 4. Assess significance of condition's influence by randomizing condition locations.***

200 A critical issue for any colocalization analysis is to determine whether the observed colocalization is
201 significantly different from what is expected by chance (Bolte and Cordelières, 2006; Fletcher et al., 2010;
202 Lagache et al., 2015). The procedure in Steps 2 and 3 for calculating f_{coloc}^{nullTR} allowed us to compare the
203 colocalization measures obtained for the data to their coincidental counterparts in the absence of a true
204 relationship between target and reference. However, a similar concern applied to the extracted influence
205 of the condition on target colocalization with reference, and this was not covered by calculating f_{coloc}^{nullTR}.

206 To address this concern, we randomized the locations of the condition objects, while keeping the
207 same number of condition objects and not altering the target or reference objects in any way (see
208 Materials and Methods and **Suppl. Figure S1**). We then repeated Steps 1-3 above. Comparison of the
209 original data colocalization measures to those calculated after condition location randomization (p_{randC}
210 or p_{randC}^{rs}) allowed us to determine whether colocalization with the condition significantly increased (or
211 decreased) the extent of target colocalization with reference.

212

213 **Generalization of conditional colocalization analysis to non-punctate objects**

214 In the above analysis scheme, we assumed that the objects were diffraction-limited punctate objects and
215 defined the distance between objects as the distance between their centers. While this covers a large
216 range of colocalization problems, including of molecules and of sub-resolution subcellular structures such

217 as clathrin-coated pits and other nanodomains (Aguet et al., 2013; Sezgin et al., 2017), many subcellular
218 structures of interest, especially as condition objects, could be larger than the resolution limit.
219 Therefore, we generalized the above scheme to the case where one out of the three object types
220 was non-punctate. For this, we introduced two modifications: (i) We replaced Gaussian fitting with image
221 segmentation to delineate objects in the non-punctate channel. (ii) We defined the distance between a
222 punctate object and a non-punctate object as the distance from the center of the punctate object to the
223 nearest pixel of the non-punctate object.
224 With this, if the non-punctate objects were the condition, the above derivations and calculations
225 were applicable as is and they yielded all five conditional colocalization measures of interest. If the non-
226 punctate objects were the reference, the above analysis scheme allowed us to calculate three out of the
227 five measures: $p(TwR)$, $p(TwR|TwC)$ and $p(TwR|TnC)$. We did not calculate the remaining measures
228 because they would require classifying larger, non-punctate reference objects as colocalized or not with
229 smaller, punctate condition objects, which is not clearly defined. For the same reason, the above analysis
230 was not generalized to non-punctate target objects, which would have to be classified as colocalized or
231 not with both punctate reference objects and punctate condition objects, both of which would be smaller
232 than the target objects in this scenario.
233
234 **Analysis scheme accurately estimates conditional colocalization measures in simulated data**
235 To assess the accuracy of our conditional colocalization analysis scheme, we tested it on simulated data
236 with known ground-truth conditional colocalization measures. To make the simulations as realistic as
237 possible, we took experimental data cell masks and simulated various colocalization scenarios within the
238 cell masks. To localize punctate objects, we selected sub-pixel coordinates within each cell mask. For non-
239 punctate objects, we used paxillin patch segmentations from our experimental data (belonging to the cell
240 masks employed). This allowed us to simulate non-punctate objects of varying sizes and shapes in a
241 realistic manner, especially in the context of our biological applications. Further simulation details are
242 described in Materials and Methods.
243 First, we validated the core colocalization analysis between two sets of objects. For the case of
244 punctate target and reference objects, we used N_T = 150, 200, 250, 300, 350, N_R = 150, 200, 250, 300,
245 350 and $p(TwR)$ = 0, 0.25, 0.5, 0.75, 1 (i.e. 125 parameter combinations). We generated 28 instances of
246 each of these parameter combinations, each in a different cell mask. Using a colocalization radius of three
247 pixels (as used for our experimental data analysis, as described below), the calculated $p(TwR)$ for each
248 parameter combination was very close to its ground-truth value, and, as expected, it was independent of

249 N_T and N_R (**Figure 2A**, left). Also as expected, the coincidental colocalization probability $p_{nullTR}(TwR)$
250 (calculated by replacing target object positions with a grid (Helmuth et al., 2010)) depended only on N_R,
251 reflecting the fraction of the cell mask area covered by the colocalization zones around the reference
252 objects (**Figure 2A**, right).

253 For the case of punctate target objects and non-punctate reference objects, we varied N_T = 150,
254 200, 250, 300, 350 and $p(TwR)$ = 0, 0.25, 0.5, 0.75, 1, while taking the reference objects from our
255 experimental data paxillin patch segmentations (i.e. 25 parameter combinations in this case). For this case
256 too, the calculated $p(TwR)$ for each parameter combination was very close to its ground-truth value, and
257 $p_{nullTR}(TwR)$ reflected the fraction of the cell area covered by the reference objects and the
258 colocalization zones around them (**Figure 2B**). These tests indicate that the core colocalization analysis
259 between two sets of objects yields accurate results for both the case of two sets of punctate objects and
260 the case of punctate target objects and non-punctate reference objects.

261 Next, we validated the conditional colocalization analysis. Here, given our observation that the
262 estimated $p(TwR)$ is equally accurate for all tested N_T and N_R (**Figure 2A, B**), we fixed N_T and N_R at 250
263 (middle of the range tested above) and only varied N_C and the various colocalization probabilities. For the
264 case of all punctuate objects, we varied N_C = 250, 300 and 350, $p(TwC)$ = 0.25, 0.5, 0.75, $p(RwC)$ = 0.25,
265 0.5, 0.75, $p(TwR|TwC)$ = 0.25, 0.5, 0.75 and $p(TwR|TnC)$ = 0.25, 0.5, 0.75 (i.e. 243 parameter
266 combinations in total). For the case of non-punctate condition objects, we took the condition objects from
267 our experimental data paxillin patch segmentations (as above, but now as condition objects instead of
268 reference objects), and varied $p(TwC)$, $p(RwC)$, $p(TwR|TwC)$ and $p(TwR|TnC)$ as above (i.e. 81
269 parameter combinations). Each of these parameter combinations was simulated 15 times using 15 cell
270 masks (and their associated paxillin patch segmentations in the case of non-punctate condition objects).
271 For each parameter combination, we compared the calculated $p(TwC)$, $p(RwC)$, $p(TwR|TwC)$ and
272 $p(TwR|TnC)$ to their input values, and the calculated $p(TwR)$, $p^{rs}\big(Tw(RwC)\big)$ and $p^{rs}\big(Tw(RnC)\big)$ to
273 their expected values (see **Eqs. S1, S4 and S5** in Materials and Methods). We found that all conditional
274 colocalization measures were estimated accurately, regardless of number and type (punctate vs. non-
275 punctate) of condition objects (**Figure 2C-G**). The equivalent results for punctate and non-punctate
276 condition objects imply that our validation test results are not limited to paxillin patch-like condition
277 objects, as used in these validation simulations, but can be generalized to condition objects of arbitrary
278 shape and size.

279

280 **Specificity: analysis scheme correctly identifies no colocalization in an experimental negative control**

281 While the above simulations verified that our analysis scheme was able to accurately estimate the
282 conditional colocalization measures, simulations might not capture some of the complexity and nuances
283 of cellular images. For example, in our simulations, objects were placed randomly within the cell mask.
284 However, molecules in a cell are often distributed in an inhomogeneous manner, leading to nonspecific
285 colocalization that is not related to any direct or indirect interactions. Furthermore, the resolution limit
286 of light microscopy, and the colocalization radius used for the analysis of diffraction-limited images, are
287 relatively large when compared to molecular dimensions. In our analyses, we employed a colocalization
288 radius of three pixels (equal to 243 nm or 267 nm depending on dataset/microscope), in order to account
289 for registration shifts between different channels and to gather enough statistics per group of objects.
290 Therefore, an important question to address was whether nonspecific colocalization might be detected in
291 the absence of any true (direct or indirect) interactions and specific relationships between the molecules
292 of interest.

293 To address this question, we applied conditional colocalization analysis to an experimental
294 negative control dataset. We performed three-color immunofluorescence (IF) imaging of TfR (transferrin
295 receptor; taken as "target"), TSAd (taken as "reference") and CHC (clathrin heavy chain; taken as
296 "condition") in endothelial cells (ECs). We employed total internal reflection fluorescence microscopy
297 (TIRFM), with a penetration depth of ~90 nm, to focus on the bottom cell surface and minimize apparent
298 colocalization from signals existing in different z-planes (**Figure 3A**). TfR is a cell surface receptor
299 responsible for binding transferrin, an iron-binding glycoprotein (Gammella et al., 2017). On the other
300 hand, TSAd is an adaptor protein that, in ECs, binds to activated VEGFR-2 (Sun et al., 2012). There are no
301 reports of association between TSAd and TfR, making this pair of molecules a good negative control. As
302 for CHC, it is a marker for clathrin-coated structures (CCSs), including clathrin-coated pits, which are
303 responsible for clathrin-mediated endocytosis, the main mechanism for TfR internalization into the cell
304 (Liu et al., 2010; Mayle et al., 2012). Thus, we would expect a certain level of association between TfR and
305 CCSs, making them relevant condition objects for conditional colocalization analysis.

306 All channels were of a punctate nature. Thus, we determined the object positions in each channel
307 with subpixel localization using Gaussian fitting (Aguet et al., 2013) (**Figure 3B-E**), and then applied the
308 conditional colocalization analysis algorithm for three sets of punctate objects. As expected, TfR exhibited
309 significant colocalization with CCSs (the condition objects) (**Figure 3F**). TSAd also exhibited significant
310 colocalization with CCSs, although less than TfR (**Figure 3F**). TSAd colocalization with CCSs was probably
311 because of its interactions with cell surface receptors such as VEGFR-2, which themselves might reside in

312 CCSs. Overall, both molecules colocalized with CCSs, giving us a sizable condition-positive group of each
313 molecule type for conditional colocalization analysis.

314 Importantly, even though both TfR and TSAd colocalized with CCSs, TfR did not exhibit any
315 significant colocalization with TSAd by any of our conditional colocalization measures (**Figure 3G**). No
316 measure was statistically distinguishable from its corresponding coincidental counterparts (nullTR and
317 randC (**Figure 3G**; blue vs. black vs. green)) and $p(TwR)$. Overall, these negative control results
318 demonstrate that conditional colocalization analysis possesses reliable specificity, correctly identifying
319 situations of no colocalization. This lends confidence to the conditional colocalization measures and the
320 colocalization relationships that they reveal.

321

322 **Sensitivity: analysis scheme captures the colocalization properties of an experimental positive control**

323 In addition to the properties of cellular images that could undermine the specificity of conditional
324 colocalization analysis, some factors might also undermine the sensitivity of the analysis, i.e. its ability to
325 detect colocalization when the co-imaged molecules are known to interact. Such factors include antibody
326 specificity and sensitivity in the case of IF and detection and segmentation errors related to image SNR
327 (including false positives and false negatives). To test the sensitivity of our conditional colocalization
328 analysis scheme, we applied it to images of molecules known to interact with each other.

329 For this, we chose three proteins that are part of focal adhesion (FA) complexes: β_1-integrin, FAK
330 (focal adhesion kinase) and paxillin (Geiger et al., 2009; Vicente-Manzanares and Horwitz, 2011). Integrins
331 are a family of cell surface receptors that bind to components of the extracellular matrix and initiate the
332 formation of FAs (Bachmann et al., 2019; Hynes, 2002). FA formation involves the activation of a series of
333 kinases, such as FAK, which in turn activates paxillin, an FA adapter protein, responsible for the scaffolding
334 and recruitment of other signaling molecules to FAs (López-Colomé et al., 2017; Mitra et al., 2005). Given
335 their mutual interactions and involvement in FA formation, activated β_1-integrin, activated FAK
336 (phosphorylated FAK or pFAK), and paxillin constituted a viable positive control for our conditional
337 colocalization analysis.

338 We performed three-color IF imaging of activated β_1-integrin, pFAK, and paxillin in ECs using
339 TIRFM (**Figure 4A-E**). For activated β_1-integrin and pFAK, we used low antibody concentrations, and
340 further bleached the images (see Materials and Methods), in order to obtain punctate signals, which were
341 detected with sub-pixel localization using Gaussian fitting (Aguet et al., 2013) (**Figure 4B, C, E**). On the
342 other hand, the paxillin signal was non-punctate, and it was segmented using intensity-based thresholding
343 (Jaqaman et al., 2016), focusing on objects larger than the diffraction limit (**Figure 4D, E**). Thus, paxillin

344 was used as a marker for FAs, which served as the condition for our analysis. Note that the incomplete
345 labeling of activated β_1-integrin and pFAK posed an additional challenge for conditional colocalization
346 analysis, as incomplete labeling is expected to reduce the extent of observed colocalization between the
347 imaged molecules.

348 Both activated β_1-integrin and pFAK exhibited significant colocalization with the paxillin patches,
349 with activated β_1-integrin showing greater colocalization than pFAK (**Figure 4F**). They also exhibited
350 significant colocalization with each other, but only for the subpopulation of pFAK that was colocalized
351 with paxillin; this was revealed by performing the conditional colocalization analysis once taking β_1-
352 integrin as target and pFAK as reference (**Figure 4G**), and once taking pFAK as target and β_1-integrin as
353 reference (**Figure 4H**). With pFAK as reference, only $p^{rs}\big(Tw(RwC)\big)$ (RwC = pFAK with paxillin) was
354 significantly greater than its coincidental counterparts and $p(TwR)$ (**Figure 4G**). Conversely, with pFAK as
355 target, only $p(TwR|TwC)$ (TwC = pFAK with paxillin) was significantly greater than its coincidental
356 counterparts and $p(TwR)$ (**Figure 4H**). Of note, in neither case was the overall colocalization probability
357 $p(TwR)$ different from its coincidental counterpart. In other words, only by identifying the proper subset
358 of pFAK – those colocalized with FAs – was it possible to capture the colocalization relationship between
359 pFAK and β_1-integrin. The pFAK molecules not colocalized with FAs were probably interacting with cell
360 surface receptors other than integrins and involved in other signaling pathways (Marlowe et al., 2016;
361 Murphy et al., 2019; Rigiracciolo et al., 2019; Sulzmaier et al., 2014).

362 These results highlight the power of conditional colocalization analysis in the face of molecular
363 and interaction heterogeneity within the cell and demonstrate its ability to quantify the context-based
364 colocalization relationships between (directly or indirectly) interacting molecules.

365

366 **Application 1: Conditional colocalization analysis reveals modulation of receptor-downstream effector**
367 **colocalization at specific membrane locations**

368 The spatial compartmentalization of molecular interactions is an emerging theme in signaling. Cell surface
369 receptors have been observed to preferentially interact with downstream effectors at particular
370 membrane microdomains, and to signal differently from different subcellular compartments (Birch et al.,
371 2021; Delos Santos et al., 2015; Eichmann and Simons, 2012; Jaqaman and Ditlev, 2021; Sorkin and von
372 Zastrow, 2009; Sungkaworn et al., 2017). Conditional colocalization analysis is ideally suited to shed light
373 on the spatial regulation and/or compartmentalization of molecular interactions (and consequently
374 signaling) within their cellular environment, in an automated and quantitative fashion.

375 To illustrate this capability, we applied conditional colocalization analysis to the receptor tyrosine
376 kinase VEGFR-2 (Vascular Endothelial Growth Factor Receptor 2) and its downstream effector TSAd (T cell
377 specific adaptor protein; also known as VEGF receptor adaptor protein (VRAP)) in the context of FAs.
378 VEGFR-2, expressed on the surface of ECs, is the main receptor for VEGF (short for VEGF-A) (Ferrara et al.,
379 2003; Simons et al., 2016). VEGFR-2 activation by VEGF triggers multiple signaling pathways, initiated by
380 the binding of multiple downstream effectors to activated VEGFR-2 (Ferrara et al., 2003; Simons et al.,
381 2016). Among the different downstream effectors, TSAd initiates a signaling cascade that modulates FA
382 turnover and cell adhesion, critically important for EC motility and angiogenic sprouting (Abedi and
383 Zachary, 1997; Birukova et al., 2009; Gordon et al., 2016; Sun et al., 2012; Wu et al., 2000). Motivated by
384 our initial observation that VEGFR-2 tends to localize near FAs (**Figure 5A**), and given that TSAd binding to
385 VEGFR-2 results in signaling to FAs, we employed conditional colocalization analysis to investigate
386 whether the interactions between VEGFR-2 and TSAd are enhanced at FAs.
387 We performed three-color IF imaging of VEGFR-2, TSAd and paxillin using TIRFM, in the absence
388 or presence of 2 nM VEGF (5 min stimulation before fixation, which robustly activates VEGFR-2 (da Rocha-
389 Azevedo et al., 2020)). The VEGFR-2 and TSAd signals were punctate and were thus localized using
390 Gaussian fitting (Aguet et al., 2013) (**Figure 5B, C**). FAs, as marked by paxillin patches, were segmented
391 using intensity-based thresholding as above (Jaqaman et al., 2016) (**Figure 5D**). Taking FAs as the
392 condition, VEGFR-2 exhibited significant colocalization with FAs, both in the absence and presence of VEGF
393 (**Figure 5E, F**). There was a mild, marginally significant increase in VEGFR-2 colocalization with FAs upon
394 stimulation by VEGF (**Figure 5F**). TSAd also exhibited significant colocalization with FAs in the absence and
395 presence of VEGF, although to a lesser extent than VEGFR-2 (**Figure 5F**).
396 For conditional colocalization analysis, taking VEGFR-2 as target and TSAd as reference, we found
397 that VEGFR-2 exhibited significant colocalization with TSAd for the subset of TSAd colocalized with FAs
398 ($p^{rs}\big(Tw(RwC)\big)$ in **Figure 5G, H**). This was the case both in the absence and presence of VEGF, with a
399 mild (albeit not statistically significant) increase in colocalization in the presence of VEGF (**Figure 5G, H**).
400 Performing the converse analysis, i.e. taking TSAd as target and VEGFR-2 as reference, maintained the
401 special status of TSAd that is colocalized with FAs: here too, TSAd exhibited significant colocalization with
402 VEGFR-2 only when TSAd colocalized with FAs ($p(TwR|TwC)$ in **Figure 5I, J**). Our observation that the
403 overall colocalization between VEGFR-2 and TSAd ($p(TwR)$ in **Figure 5G-J**) was not significant under any
404 circumstances highlights the need for conditional colocalization analysis and the unique information that
405 it reveals, which would be lost with traditional colocalization analysis and other ensemble/bulk
406 approaches.

407 To determine whether the effect of FAs on VEGFR-2 and TSAd colocalization was specific to FAs,
408 we performed conditional colocalization analysis of VEGFR-2 and TSAd in the context of clathrin-coated
409 structures (CCSs) and compared the analysis results to those in the context of FAs. VEGFR-2 is internalized
410 via clathrin-mediated endocytosis in both ligand-dependent and ligand-independent manners
411 (Basagiannis et al., 2016; Lampugnani et al., 2006). VEGFR-2 can also continue downstream signaling after
412 internalization (Lanahan et al., 2010; Simons et al., 2016). These properties made CCSs a viable condition
413 object with which we would expect VEGFR-2 to colocalize, possibly together with downstream effectors.
414 We performed three-color IF imaging of VEGFR-2, TSAd and CHC using TIRFM, in the absence and
415 presence of VEGF as above. As all channels were punctate, all objects were localized using Gaussian fitting
416 (Aguet et al., 2013) (**Suppl. Figure S2A-E**). Both VEGFR-2 and TSAd colocalized with CCSs as the condition
417 (**Suppl. Figure S2F**). We performed conditional colocalization analysis taking VEGFR-2 as target and TSAd
418 as reference and vice versa (**Suppl. Figure S2G-J**). No colocalization measures were significant, except for
419 the probability of VEGFR-2 (target) to colocalize with TSAd (reference) if VEGFR-2 was colocalized with
420 CCSs (condition), in the presence of VEGF ($p(TwR|TwC)$ in **Suppl. Figure S2H**). Thus, overall, CCSs exert
421 much less influence on the colocalization between VEGFR-2 and TSAd than FAs. Furthermore, their
422 influence is different from that of FAs: In the case of FAs, colocalization was enhanced for the subset of
423 TSAd at FAs. In the case of CCSs, colocalization was enhanced for the subset of VEGFR-2 at CCSs.
424 Altogether, these analyses indicate that the colocalization relationship between VEGFR-2 and
425 TSAd varies depending on their location within the plane of the plasma membrane. In particular, it is
426 influenced in a specific, positive manner by the colocalization of TSAd with FAs, which are functionally
427 relevant for VEGFR-2 signaling downstream of TSAd. To the extent that colocalization is reflective of
428 interactions between VEGFR-2 and TSAd, this raises the question of what is special about the subset of
429 TSAd at FAs, such that VEGFR-2 exhibits increased colocalization with it. One possibility is the presence of
430 other interaction partners or feedback from downstream signaling that stabilize the interactions between
431 TSAd and VEGFR-2. Performing further conditional colocalization analysis with other interaction partners
432 and combining it with perturbation of the different molecular players is expected to help determine the
433 molecular mechanisms behind this increase in VEGFR-2-TSAd interactions at FAs. Importantly, the
434 increased interactions most likely facilitate VEGFR-2 signaling in the right place at the right time to
435 regulate cellular adhesion and migration in response to VEGF.
436
437 **Application 2: Conditional colocalization analysis reveals colocalization interdependencies between**
438 **three molecules**

439 In the cell, molecules are engaged in networks of interactions with many other molecules, leading to the
440 formation of complexes, clusters and condensates that are important for cell signaling and other cellular
441 functions (Gingras et al., 2019; Jaqaman and Ditlev, 2021; Yanez-Mo et al., 2009). Determining which
442 molecules interact directly, and which interact indirectly through mediator molecules, is a critical step
443 toward understanding the molecular mechanisms underlying the formation of these higher-order
444 molecular assemblies. Through its analysis of the colocalization relationships between multiple molecules,
445 conditional colocalization analysis is ideally suited to shed light on the hierarchy of intermolecular
446 interactions within their cellular context.

447 This application of conditional colocalization analysis differs in purpose from the previous
448 application. In the previous application, the condition objects were pre-determined subcellular
449 structures/membrane microdomains (e.g. FAs or CCSs), and the question was whether these domains (the
450 condition) played any role in the colocalization of two molecules. In this application, the goal is to identify
451 the condition itself, i.e. the molecule that may act as a mediator between the other two.

452 To illustrate this capability, we applied conditional colocalization analysis to the three cell surface
453 proteins CD36, β_1-integrin and CD151. CD36 is a scavenger receptor expressed on the surface of many cell
454 types, where it binds diverse ligands and is implicated in various (patho-)physiological processes, such as
455 angiogenesis, atherosclerosis, Alzheimer's disease and immunity (Silverstein and Febbraio, 2009). CD36
456 clustering and engagement within multimolecular complexes containing integrins (particularly those
457 containing the β_1 subunit) and tetraspanins (CD9, CD81 and/or CD151, dependent on cell type) are
458 thought to be important for its signaling function, as the two short intracellular domains of CD36 lack any
459 known signaling motifs (Githaka et al., 2016; Heit et al., 2013; Huang et al., 2011; Kazerounian et al., 2011;
460 Miao et al., 2001; Primo et al., 2005; Thorne et al., 2000). However, these integrins and tetraspanins
461 interact with each other and with other membrane proteins (Charrin et al., 2009; Yauch et al., 2000; Zhang
462 et al., 2009), making it difficult to determine the molecular mechanisms underlying their interactions with
463 CD36 and their contribution to CD36 signaling.

464 We reasoned that conditional colocalization analysis could shed light on the hierarchy, if any, in
465 the interactions between CD36, integrins and tetraspanins. In ECs, β1-integrin and the tetraspanin CD151
466 have been shown to co-immunoprecipitate with CD36 (Kazerounian et al., 2011; Primo et al., 2005). Thus,
467 we asked whether CD36 interacts separately (or independently) with β1-integrin and CD151, or whether
468 its interactions with one depend on the other. Addressing this question with traditional knockout or
469 knockdown approaches would not be straightforward, given the essential role that integrins play in cell
470 physiology and the redundancy between tetraspanins (Charrin et al., 2009; Winograd-Katz et al., 2014).

471 We performed fixed cell imaging of CD36, β1-integrin and CD151 on the surface of ECs using
472 TIRFM (**Figure 6A-E**), followed by conditional colocalization analysis. For these experiments we used an
473 antibody that recognizes total β1-integrin, regardless of its activation state (Byron et al., 2009) (in contrast
474 to the positive control application above). Considering all pairs of target and reference objects (no
475 conditional analysis yet), $p(TwR)$ revealed significant overall colocalization between CD151 and β1-
476 integrin (both ways), but not between CD36 and β1-integrin or CD36 and CD151 (**Figure 6F**). However,
477 performing conditional colocalization analysis, and taking β1-integrin as the condition, the subset of CD36
478 colocalized with β1-integrin exhibited significant colocalization with CD151 ($p(TwR|TwC)$ in **Figure 6G**).
479 With CD151 as the condition, the subset of CD36 colocalized with CD151 exhibited slightly elevated,
480 marginally significant, colocalization with β1-integrin ($p(TwR|TwC)$ in **Figure 6H**; p-value = 0.1). Neither
481 the fraction of β1-integrin nor the fraction of CD151 colocalized with CD36 was significant, regardless of
482 the condition (**Suppl. Figure S3A, B**). This highlights the necessity for object-based colocalization analysis
483 that allows for non-reciprocal colocalization relationships given the different abundance of different
484 molecules. Finally, taking CD36 as the condition did not enhance the already significant colocalization
485 between β1-integrin and CD151 (**Suppl. Figure S3C, D**).
486 The CD36-independent colocalization between β1-integrin and CD151 is consistent with previous
487 work that found direct association between β1-integrin and CD151 through their extracellular domains
488 (Yauch et al., 2000). Our data suggest that CD36 interactions with β1-integrin bring CD36 to a complex
489 that also contains CD151, through the latter's interactions with β1-integrin. However, because the overall
490 probability of CD36 colocalization with β1-integrin ($p(TwR)$ in **Figure 6F**) is not significant, this suggests
491 that the interaction of CD36 with β1-integrin also requires a mediator/stabilizer. This could be CD151,
492 given the slight elevation of colocalization of CD36 with β1-integrin if CD36 is colocalized with CD151
493 ($p(TwR|TwC)$ in **Figure 6H**), or some other molecule, or lipid nanodomain, not investigated in our study
494 (Silverstein and Febbraio, 2009). The lack of significant pairwise colocalization between CD36 and β1-
495 integrin could also be the result of labeling all β1-integrins in our study, regardless of the α-integrin
496 partner, while CD36 may be interacting with particular αβ heterodimers (most likely $\alpha_6\beta_1$ and/or $\alpha_3\beta_1$
497 (Miao et al., 2001; Thorne et al., 2000)). Altogether, these analyses reveal that β1-integrin and CD151
498 colocalize together independently of CD36, while CD36 colocalizes with them together, as a complex, with
499 β1-integrin acting as a major mediator/stabilizer between CD36 and CD151.
500

501 ## Discussion

502 We have developed a new approach, conditional colocalization analysis, to assess the colocalization
503 relationships and hierarchies between three molecular entities from multicolor microscopy images. Going
504 beyond the question of whether two entities colocalize, it addresses the question whether the
505 colocalization between two entities is increased or decreased by a third entity. We have demonstrated its
506 specificity and sensitivity, and showcased its application to two different biological questions, one
507 regarding the regulation of receptor-downstream effector interactions at specific plasma membrane
508 locations, and one regarding the hierarchy of molecular interactions in multimolecular complexes. The
509 source code for performing conditional colocalization analysis, along with detailed instructions for running
510 it, is available at https://github.com/kjaqaman/conditionalColoc.

511 Conditional colocalization analysis of multicolor images offers an approach to shed light on
512 interaction dependencies, hierarchies and regulation within the native, unperturbed environment of
513 these interactions. It complements the classic approach of system perturbation to probe these questions
514 in at least two ways. First, because it extracts information from the unperturbed system, it can provide
515 unique insight in cases where molecular perturbations have side effects that complicate the interpretation
516 of results, or where there is functional redundancy between molecules, in which case one molecule may
517 compensate for another upon perturbation, thus masking the perturbed molecule's true function(s)
518 (Wagner, 2000; Zhang, 2012). Second, it enables the initial dissection of a system to gather evidence for
519 the important players in regulating the interactions of interest, thus guiding later experiments involving
520 molecular perturbations. Applying conditional colocalization analysis to super-resolution microscopy
521 images instead of conventional microscopy images will bring the analyzed inter-object distances closer to
522 molecular dimensions, thus deepening the insight that conditional colocalization analysis may provide
523 about molecular interactions and their regulation (Huang et al., 2009; Sahl et al., 2017).

524 The information that conditional colocalization analysis of multicolor images yields about
525 molecular interactions is difficult to obtain through other methods commonly employed to detect
526 molecular interactions in their cellular context, such as Förster Resonance Energy Transfer (FRET) and
527 Bimolecular Fluorescence Complementation (BiFC) (Romei and Boxer, 2019; Sun et al., 2013). Although
528 some extensions have enabled the detection of triple interactions with FRET and BiFC (Kwaaitaal et al.,
529 2010; Scott and Hoppe, 2015), these methods are mostly designed to yield signal only when the
530 interaction of interest takes place. In other words, they primarily address the question of whether an
531 interaction takes place or not. They do not allow the calculation of a probability of interacting, and thus
532 they cannot be used to analyze the modulation of interactions without system perturbation.

While our application of conditional colocalization analysis has been focused on the molecular and macromolecular scale, this analysis approach is applicable to any biological system, as long as at least two out of the three imaged entities can be treated as punctate objects represented by their center coordinates. These objects do not have to be diffraction-limited; as long as they are approximately circular and of homogeneous size, their radius can be incorporated into the colocalization radius between objects. As for non-punctate objects, they can take any form or shape, as long as they are segmented properly, e.g. using ridge detection for curvilinear objects (Kittisopikul et al., 2020) or using deep learning approaches (Lucas et al., 2021). In addition, conditional colocalization analysis can be tailored to particular biological questions through question-specific selection of the objects analyzed (e.g. objects from a particular subcellular region, or objects of a certain size or shape). For example, our observation that β_1-integrin at FAs does not show enhanced colocalization with pFAK hints at the transient residency of pFAK at FAs, which depends on the size of FAs (Kleinschmidt and Schlaepfer, 2017; Le Dévédec et al., 2012). Thus, it may be informative to analyze β_1-integrin-pFAK colocalization in the context of different sizes of FAs.

Conceptually, conditional colocalization analysis can be extended in multiple ways. The same analysis, as currently implemented, can be applied to 2D live cell imaging, to determine the modulation of colocalization relationships over time, e.g. in response to a cellular stimulus. The analysis can be also readily extended to 3D, as long as there is sufficient axial resolution. Light-sheet microscopy with isotropic resolution would be ideally suited for this purpose (Power and Huisken, 2017). Finally, the analysis can be extended to analyze the colocalization relationships and hierarchies between more than three entities, as long as informative conditional probabilities and related measures can be defined. As extending the analysis to more than three colors will increase the total number of possible object combinations, the analysis procedure in this case may be iterative, to help identify biologically relevant object combinations. All in all, conditional colocalization analysis is a broadly-applicable method for the analysis of multicolor microscopy images. By dissecting the colocalization relationships between multiple molecular entities, it helps with the dissection of the complex landscape of multimolecular interactions in the cell.

Materials and Methods

Plasmids

563 A plasmid encoding CD36-fused at the N-terminus to HaloTag (Halo-CD36) was generated by PCR-cloning
564 the amplification of HaloTag coding sequence (primers HaloTag-For and HaloTag-Rev detailed below
565 (IDTDNA, Coralville, IA)) from pFN21K HaloTag® CMV Flexi® Vector (Promega, Madison, WI), followed by
566 ligation in place of the mApple sequence in the mApple-CD36-C-10 vector (plasmid # 54874, Addgene,
567 Watertown, MA (Githaka et al., 2016)), using restriction enzymes AgeI and BglII. Selected plasmid was
568 verified by Sanger sequencing.
569 *HaloTag-For primer:*
570 CATCCAGCGGGGATCCACCGGTCATGGCAGAAATCGGTACTGGCTTTCCATTCG
571 *HaloTag-Rev primer:*
572 CCACTGCTGCCAGATCTCATGGCGATCGCGTTATCGCTCTG
573
574 **Cell culture and plating**
575 Human Telomerase (hTERT)-immortalized microvascular endothelial cells isolated from human foreskin
576 (TIME cells, ATCC, Manassas, VA) were grown in ATCC's vascular cell basal medium supplemented with
577 microvascular endothelial cell growth kit-VEGF and 12.5 µg/mL blasticidine (Sigma-Aldrich, St Louis, MO)
578 for 48 h at 37°C + 5% CO_2 until reaching 80-90% confluence. At confluence, cells were passaged and
579 5.4×10^4 cells were plated on fibronectin-coated (10 µg/ml, MilliporeSigma, Burlington, MA), base/acid
580 cleaned, 0.17 mm (#1.5) glass bottom dishes (14 mm glass diameter, MatTek, Ashland, MA) for 18 h prior
581 to experiments.
582
583 **Transfection of Halo-CD36 in TIME cells**
584 The Halo-CD36 plasmid was transiently transfected into TIME cells. Briefly, 5×10^6 TIME cells (passages 14
585 to 21) were suspended in serum and antibiotic-free DMEM (ThermoFisher, Waltham, MA) and incubated
586 with Halo-CD36 (1 µg) and UTR (Universal Transfection Reagent, Sigma) at 37°C for 20 min, following
587 which the transfection mixture was added to a T-25 flask filled with complete DMEM medium. Transfected
588 cells were plated on fibronectin-coated dishes, as described above, on day 1 post-transfection. Cells were
589 imaged on day 2 post-transfection.
590
591 **Sample preparation for fluorescence imaging**
592 For all samples except for CD36/β_1-integrin/CD151, plated cells were washed once in wash buffer (HBSS
593 + 1 mM HEPES and 0.1% NGS) to remove culture medium, and then incubated with HBSS containing or
594 not 2 nM VEGF-A_{165} (Genscript, Piscataway, NJ) for 5 min at 37°C. Incubation solution was then removed

595 and cells were fixed with a 3.2% Paraformaldehyde solution made in PBS (Electron Microscopy Sciences,
596 Hatfield, PA) for 15 min at RT. Samples were then washed three times (5 min each) at RT with wash buffer,
597 then permeabilized for 1 min with cold 0.01% Triton X-100 solution made in PBS. After three washes,
598 samples were blocked for 15 min in blocking buffer (1% BSA, 5% NGS in wash buffer) and then incubated
599 for 1 hr with primary antibodies (**Table 1**) at RT. After three washes, samples were incubated with
600 secondary antibodies (**Table 1**) for 15 min at RT. After three more washes, they were then incubated with
601 AlexaFluor647-conjugated primary antibodies (**Table 1**) for 15 min at RT. Finally, after three subsequent
602 washes, dishes were incubated with imaging buffer (Oxyfluor 1%, Glucose 0.45%, Trolox 2 nM) in order to
603 reduce photobleaching.

604 For CD36/β_1-integrin/CD151, CD36 transfected cells (day 2 post-transfection) were rinsed with
605 sterile DPBS and incubated with 50 nM JF549-Halo ligand (generous gift from Dr. Luke Lavis, Janelia
606 Research Campus, Ashburn, VA) for 15 min in complete culture medium. This was followed by 3 quick
607 washes in DPBS and then samples were incubated for 15 min in dye free complete culture medium.
608 Incubations were at 37˚C + 5% CO_2. Following CD36 labelling, samples were washed once in wash buffer
609 and fixed with a 4% Paraformaldehyde + 0.1% Glutaraldehyde (Electron Microscopy Sciences, Hatfield,
610 PA) solution made in PBS, for 20 min at 4°C, in the dark. Freshly prepared quenching solution (0.1% NaBH4,
611 Oakwood Chemical, Estill, South Carolina) was added immediately after fixation and cells were incubated
612 for 7 min. Samples were then washed 3 times (5 min each) at RT with wash buffer. Samples were blocked
613 for 30 min in blocking buffer and then incubated for 1 hr with a mouse primary antibody against β_1-integrin
614 at RT (**Table 1**). After three washes, samples were incubated with an AlexaFluor488-conjugated goat anti-
615 mouse secondary antibody (**Table 1**) for 15 min at RT. After three more washes, they were then incubated
616 with AlexaFluor647-conjugated primary antibody against CD151 (**Table 1**) for 30 min at RT. Finally, after
617 three subsequent washes, dishes were incubated with imaging buffer before imaging.
618

Antibody	**Host, Clonality**	**Manufacturer (identifier)**	**Dilution used**
Unconjugated primary			
Anti- TfR	Rabbit, polyclonal	Abcam, ab84036	1:200
Anti-TSAd (OTI4F3)	Mouse, monoclonal	Invitrogen, MA5-25894	1:100
Anti-β_1-integrin (activated) (P4G11)	Mouse, monoclonal	Sigma-Aldrich, MAB1951	1:10000
Anti-pFAK (pY397) (EP2160Y)	Rabbit, Monoclonal	Abcam, ab81298	1:10000
Anti-VEGFR-2 (55B11)	Rabbit, Monoclonal	Cell Signaling Technology, #2479	1:400
Anti-β_1-integrin (neutral) (K20)	Mouse, Monoclonal	Beckman Coulter, IM0791U	1:75000

Conjugated primary			
Alexa Fluor® 647 Anti-CD151 (11G5a)	Mouse, Monoclonal	Abcam, ab199200	1:500
Alexa Fluor® 647 Anti-Paxillin (Y113)	Rabbit, Monoclonal	Abcam, ab246719	1:100
Alexa Fluor® 647 Anti-CHC (X22)	Mouse, Monoclonal	Invitrogen, MA1-065-A647	1:2000
Secondary			
Alexa Fluor® 488 Anti-Mouse IgG secondary	Goat, polyclonal	Invitrogen, A-11029	1:1000
Alexa Fluor® 546 Anti-Rabbit IgG secondary	Goat, polyclonal	Invitrogen, A-11010	1:1000
Alexa Fluor® 488 Anti-Rabbit IgG secondary	Goat, polyclonal	Invitrogen, A-11008	1:10000
Alexa Fluor® 546 Anti-Mouse IgG secondary	Goat, polyclonal	Invitrogen, A-11003	1:10000

Table 1. Primary and secondary antibodies and their dilutions used for IF imaging.

Total internal reflection fluorescence microscopy (TIRFM) imaging

For the TfR/TSAd/CHC, activated β1-integrin/pFAK/Pax, VEGFR2/TSAd/CHC and VEGFR2/TSAd/Pax datasets, cells were imaged at 37°C using an Olympus IX83 TIRF microscope equipped with a Z-Drift Compensator and a UAPO 100X/1.49 NA oil-immersion TIRF objective (Olympus, Center Valley, PA). The microscope was equipped with an iXon 888 1k × 1k EMCCD Camera (Andor - Oxford Instruments, Concord, MA). With an additional 1.6X magnification in place, the pixel size in the recorded image was 81 nm × 81 nm. Using the Olympus CellSens software, excitation light of 640 nm, 561 nm and 491 nm from an Olympus CellTIRF-4Line laser system was directed to the sample at a penetration depth of 90 nm by a TRF8001-OL3 Quad-band dichroic mirror. Fluorescence of different wavelengths was collected, filtered with emission filters of ET520/40m, ET605/52m and ET705/72m (Chroma, Bellows Falls, VT), and projected onto different sections of the camera chip by an OptoSplit III 3-channel image splitter (Cairn Research, Faversham, Kent, UK). The different channels were excited and recorded sequentially, in the order 640, then 561, then 491. Images were acquired with MetaMorph (Molecular Devices, San Jose, CA). Camera EM gain was set to 100 for all acquisitions.

For all molecule combinations mentioned above except for activated β_1-integrin/pFAK/Pax, each channel was imaged once using an exposure time of 99 ms and a laser power of 3.6, 6.4 and 5.9 mW at the coverslip (measured with a Thorlabs power meter at an incident angle of 0°) for 491 nm, 561 nm and 640 nm, respectively. As for the activated β_1-integrin/pFAK/Pax combination, even with the high antibody

640 dilutions employed, the β_1-integrin and pFAK images were not always punctate. To get reliably punctate
641 images, β_1-integrin and pFAK were imaged in streaming mode for 300 frames (at 10 Hz), with laser power
642 increased to 5.4 mW for the 491 channel and 9.6 mW for the 561 channel, in order to photobleach the
643 signal. The last frame of each stream, where the β_1-integrin and pFAK signals were largely punctate, was
644 then used as the image for β_1-integrin and pFAK detection and colocalization analysis. Paxillin (the 640
645 channel) was imaged only once, as with the other molecule combinations.

646 For the CD36/β1-integrin/CD151 dataset, cells were imaged at 37°C using an S-TIRF system
647 (Spectral Applied Research, via BioVision Technologies, Exton, PA) mounted on a Nikon Ti-E inverted
648 microscope with Perfect Focus and a CFI Apo 60X/1.49 NA oil-immersion TIRF objective (Nikon
649 Instruments, Melville, NY), equipped with an Evolve EMCCD camera (Photometrics, Tucson, AZ). A custom
650 3X tube lens was employed to achieve an 89 nm × 89 nm pixel size in the recorded image. Sequential
651 illumination by a 488 nm diode laser (Coherent), a 561 nm diode pumped solid state laser (Cobolt), and a
652 637 nm diode laser (Coherent) was achieved through an ILE laser merge module (Spectral Applied
653 Research), with 488 nm, 561 nm and 637 nm laser powers of 3.65, 13.2 and 10.6 mW, respectively, at the
654 coverslip (measured with a Thorlabs power meter at an incident angle of 0°). The penetration depth was
655 set to 100 nm via the Diskovery platform control (Spectral Applied Research). Three-channel images were
656 acquired with MetaMorph (Molecular Devices, San Jose, CA), with 100 ms exposure per image, using an
657 EM gain of 100. Emission filters of ET520/40m, ET605/52m and ET705/72m (Chroma, Bellows Falls, VT)
658 were employed.

659 For every three-channel image or movie, a brightfield snapshot of the imaged cell region was also
660 acquired, in order to aid with manual delineation of the region of interest (ROI) mask for the ensuing
661 analysis.

662

663 **Computing environment.** All image and data analysis and simulation tasks were performed in Matlab
664 R2020a (The MathWorks, Natick, MA). All employed code and software packages are compatible with
665 Matlab R2020a on a Linux 64-bit operating system. Images were loaded into Matlab using Bio-Formats
666 (Linkert et al., 2010).

667

668 **Punctate object detection**

669 Punctate objects were detected using the "point-source detection" particle detection algorithm in u-track
670 (https://github.com/DanuserLab/u-track) (Aguet et al., 2013; Jaqaman et al., 2008). In brief, the algorithm
671 consists of two steps: (i) a filtering step to determine pixels likely to contain objects, and (ii) a Gaussian

fitting step to determine the object positions with sub-pixel localization. With the appropriate, wavelength-dependent standard deviation, a two-dimensional Gaussian is a good approximation of the microscope's point spread function (Thomann et al., 2002; Zhang et al., 2007). Largely default parameter values were used, except for the alpha-value for determining object detection significance by comparing the fitted Gaussian amplitude to the local background noise distribution (**Table 2**). The alpha-value was chosen based on visual assessment of the detection results, with the goal of minimizing both false positives (superfluous detections) and false negatives (missed particles). The number of objects detected within the ROI for each dataset is listed in **Table 3**.

	Channel wavelength	PSF sigma (pixels, nm)	Parameters
TfR/TSAd/CHC			
TfR	561	1.4, 113	Alpha: 0.01, all others: default.
TSAd	488	1.2, 97	Alpha: 0.01, all others: default.
CHC	640	1.58, 128	Alpha: 0.05, all others: default.
activated β1-integrin/pFAK/Pax			
activated β1-integrin	561	1.4, 113	Alpha: 0.01, all others: default.
pFAK	488	1.2, 97	Alpha: 0.01, all others: default.
Pax	640	N/A	N/A
VEGFR-2/TSAd/CHC			
VEGFR-2	561	1.4, 113	Alpha: 0.05, all others: default.
TSAd	488	1.2, 97	Alpha: 0.01, all others: default.
CHC	640	1.58, 128	Alpha: 0.05, all others: default.
VEGFR-2/TSAd/Pax			
VEGFR-2	561	1.4, 113	Alpha: 0.05, all others: default.
TSAd	488	1.2, 97	Alpha: 0.01, all others: default.
Pax	640	N/A	N/A
CD36/β1-integrin/CD151			
CD36	561	1.4, 113	Alpha: 0.01, all others: default.
β1-integrin	488	1.2, 97	Alpha: 0.01, all others: default.
CD151	640	1.58, 128	Alpha: 0.05, all others: default.

Table 2. Three-channel imaging and detection of indicated molecule combinations. PSF, point spread function. Shown are the parameters of "point-source detection" that vary between channels and datasets. Two other parameters that change (namely "Max Fit Adjust" and "Fit Window Size") are not shown because they were given their default values of 2×PSF sigma and 4×PSF sigma, respectively. The paxillin (Pax) channel has N/A parameters because it was not detected using point-source detection due to its non-punctate nature.

Dataset (Channels 1/2/3 or 561/488/640)	Channel 1 objects per ROI [min max] avg	Channel 2 objects per ROI [min max] avg	Channel 3 objects per ROI [min max] avg	ROI area (pixels) [min max] avg	Segmented patch area (pixels) [min max] avg
TfR/TSAd/CHC	[151 660] 368	[80 506] 214	[233 751] 490	[85,190 219,960] 156,800	N/A
β_1-Integrin/pFAK/ Pax	[157 804] 371	[424 1,561] 910	[47 178] 101	[61,570 234,760] 132,950	[87 159] 114
VEGFR-2/TSAd/ Pax	[357 1,194] 754	[174 663] 358	[8 218] 135	[93,880 231,610] 158,340	[73 140] 96
VEGFR-2/TSAd/ CHC	[352 1,134] 695	[200 639] 415	[284 928] 568	[62,510 202,080] 144,870	N/A
CD36/β_1-Integrin/ CD151	[34 914] 192	[191 1,871] 715	[61 739] 254	[27,760 209,170] 92,783	N/A

Table 3. Number of objects per ROI, ROI area and segmented patch area (where applicable) for the various experimental datasets.

Non-punctate object segmentation

Paxillin patches ("non-punctate objects") were segmented using an intensity threshold to separate foreground from background. The threshold was determined for each image individually. It was taken as the 90th percentile of each image's intensity distribution after noise filtering (using a Gaussian kernel with standard deviation = 1 pixel) and local background subtraction. Local background was estimated for each image by filtering it with a Gaussian kernel with standard deviation = 10 pixels. The threshold was then applied to the noise-filtered and background-subtracted image to segment the paxillin patches. Patches with an area of at least 30 pixels were retained for further analysis. The number of segmented patches within the ROI and their areas are listed in **Table 3**.

Region of interest (ROI) mask segmentation

ROI masks, covering the imaged area of each cell of interest, were delineated manually. For TfR/TSAd/CHC, VEGFR-2/TSAd/CHC and CD36/β1-integrin/CD151, delineation was based on the brightfield image. For VEGFR-2/TSAd/Pax and beta1 integrin/pFAK/Pax, delineation was based on the brightfield image as well as paxillin and pFAK (where imaged).

Core algorithm to calculate colocalization fraction of target with reference

Our implementation closely followed the original algorithm proposed in (Helmuth et al., 2010). In brief, for punctate target and reference objects, the distance between any two objects was defined as the

712 Euclidean distance between their estimated positions (centers). For punctate target and non-punctate
713 reference objects, the distance was defined as the Euclidean distance between the estimated position
714 (center) of the target object and the closest pixel in the segmentation of the non-punctate reference
715 object. With this, a target object was considered to be colocalized with a reference object if the distance
716 between it and its nearest neighbor reference object was smaller than a user-defined threshold
717 ("colocalization radius"). The colocalization radius accounted for various experimental considerations,
718 such as registration shifts between channels, segmentation accuracy, etc. The fraction of target
719 colocalized with reference (f_{coloc}) was then calculated as the ratio of the number of target objects
720 colocalized with reference objects to the total number of target objects.

721 To calculate the coincidental colocalization fraction of target with reference (f_{coloc}^{nullTR}) given the
722 cellular context, in particular the number and spatial distribution of reference objects within the ROI mask,
723 we followed (Helmuth et al., 2010) and replaced the target positions with a grid of positions covering the
724 whole ROI. Specifically, we used each pixel within the ROI as one grid point (i.e. target position), and
725 repeated the above distance calculations, classification and fraction calculation.

726

727 **Position randomization of condition objects within the ROI mask**

728 To calculate the conditional colocalization probabilities expected by chance, i.e. in the absence of any true
729 influence of the condition objects on target-reference colocalization, the condition objects were
730 randomized within the ROI mask. In the case of punctate condition objects, to ensure that none of the
731 randomly chosen locations were too close to the ROI mask boundary, the ROI mask was first eroded using
732 a square structuring element with size equal to the colocalization radius plus three pixels (i.e. six pixels in
733 our applications). The new condition object locations were then chosen within the eroded ROI mask, using
734 the same number of condition objects as in the original.

735 In the case of non-punctate condition objects, we conserved not only the number of objects, but
736 also the shape of each object. To optimize the selection of random locations, condition objects in this case
737 were placed in random locations sequentially, starting with the largest object, and going down to the
738 smallest object. The idea behind this order was that it was easier to place small objects between large
739 objects than the other way around. Once an object was placed, the pixels it occupied were removed from
740 the ROI mask, as those pixels were no longer available for any other object (**Suppl. Figure S1**). In addition,
741 before placing each object, the mask was eroded using a disk structing element with radius equal to the
742 average radius of the object being placed (**Suppl. Figure S1**). The purpose of this was to avoid placing any
743 new object too close to already-placed objects (leading to overlap) or to the ROI mask boundary (leading

744 to part of the object being outside the ROI mask). With this strategy, we were able to randomize the
745 locations of non-punctate condition objects within the ROI mask while avoiding any overlap between
746 them, and while avoiding the scenario of not enough contiguous space to place larger objects (a scenario
747 that happened often when smaller objects were placed before larger objects).
748
749 **Validation simulations**
750 As mentioned in Results, the validation simulations were performed within cell ROI masks taken from our
751 experimental data, to keep the simulations as realistic as possible. Each mask was used as a repeat for
752 each parameter combination. Cell masks were eroded using a square element with side length = 10 pixels
753 to avoid molecules being positioned too close to the cell edge.
754 ***Punctate target objects and non-punctate reference objects.*** To simulate non-punctate reference
755 objects, the paxillin patch segmentations belonging to the employed cell masks were used as reference
756 objects. Then, based on the input $p(TwR)$, target objects were divided into colocalized or not colocalized
757 with reference objects. Target objects colocalized with reference objects were placed 0-2 pixels from the
758 boundaries of the reference objects with which they were associated. Target objects not colocalized with
759 reference objects were placed at random coordinates within the eroded cell mask, excluding the pixels
760 belonging to reference objects. For this, the reference objects were dilated using a square element with
761 side length = 10 pixels to exclude the colocalization area around each reference object when placing not-
762 colocalized target objects.
763 ***Punctate target and reference objects.*** These simulations followed the strategy described above
764 for non-punctate reference objects. The only difference was that they did not use the experimental
765 paxillin patch segmentations for reference objects. Instead, reference objects were placed at random
766 coordinates within the eroded cell mask, and a binary image was created where pixels of value one
767 represented the positions of reference objects. These masks were the starting point for the simulations
768 as described for the previous case.
769 ***Punctate target and reference objects, with non-punctate condition objects.*** As with the case
770 above of non-punctate reference objects, the paxillin patch segmentations belonging to the employed cell
771 masks were used for the simulations, but this time as condition objects. Based on the input $p(TwC)$ and
772 $p(RwC)$, target and reference objects were divided into condition-positive and condition-negative
773 groups. Condition-positive reference objects were placed 0.2 pixels away from the boundaries of the
774 condition objects with which they were associated. This very close placement was motivated by practical
775 considerations; it made it easier to place target objects (as described next) close to both a reference object

776 and a condition object when needed, as being placed close to one almost guaranteed being placed close
777 to the other. Condition-negative reference objects were placed at random coordinates within the eroded
778 cell mask, excluding the pixels belonging to condition objects after dilating them using a square element
779 with side length = 10 pixels.

780 To place target objects, they were subdivided further. First, based on $p(TwR|TwC)$, the
781 condition-positive target objects were divided into colocalized or not colocalized with reference objects.
782 Condition-positive target objects colocalized with reference objects were placed 0-2 pixels from
783 condition-positive reference objects. Given the placement scheme for condition-positive reference
784 objects, this almost guaranteed that the target objects were colocalized with condition objects as well.
785 Condition-positive target objects not colocalized with reference objects were placed 0-2 pixels from the
786 boundaries of condition objects, after eliminating the boundary pixels associated with reference objects.
787 Second, based on $p(TwR|TnC)$, condition-negative target objects were divided into colocalized or not
788 with reference objects. Condition-negative target objects colocalized with reference objects were placed
789 0-2 pixels from condition-negative reference objects, which largely placed them far from condition objects
790 as well. Condition-negative target objects not colocalized with reference objects were placed at random
791 coordinates within the eroded cell mask, excluding the pixels belonging to condition objects and reference
792 objects, both after dilation using a square element with side length = 10 pixels.

793 ***Punctate target, reference and condition objects.*** These simulations followed the strategy
794 described above for non-punctate condition objects. The only difference was that they did not use the
795 experimental paxillin patch segmentations for condition objects. Instead, condition objects were placed
796 at random coordinates within the eroded cell mask, and a binary image was created where pixels of value
797 one represented the positions of condition objects. These masks were the starting point for the
798 simulations as described for the previous case.

799

800 **Derivation of expected colocalization measures from simulation input parameters**

801 In our simulations, $p(TwC)$, $p(RwC)$, $p(TwR|TwC)$ and $p(TwR|TnC)$ were explicitly defined as input
802 parameters. For validation, their values as calculated by our conditional colocalization analysis were
803 compared directly to their input values. The remaining two conditional colocalization measures,
804 $p^{rs}\big(Tw(RwC)\big)$ and $p^{rs}\big(Tw(RnC)\big)$, and the overall colocalization probability $p(TwR)$, were not
805 explicitly defined. Thus, for validation, their calculated values were compared to their expected values, as
806 derived from the input $p(TwC)$, $p(RwC)$, $p(TwR|TwC)$ and $p(TwR|TnC)$.

807 The expected value of $p(TwR)$ was calculated from the input parameters in a straightforward
808 manner using the law of total probability:

809 $$p(TwR) = p(TwR|TwC)p(TwC) + p(TwR|TnC)p(TnC).$$

810 $$= p(TwR|TwC)p(TwC) + p(TwR|TnC)\big(1 - p(TwC)\big). \quad \text{(S1)}$$

811 To calculate the expected values of $p^{rs}\big(Tw(RwC)\big)$ and $p^{rs}\big(Tw(RnC)\big)$, we assumed one
812 simplifying relationship between objects (**Assumption 1**), an assumption that was satisfied in our
813 simulations (see above).

> **Assumption 1:** If a target object and a reference object are colocalized, then either both are colocalized with a condition object, or neither is colocalized with a condition object.

814 With **Assumption 1**, and given the relationships between the different target subgroups (**Figure**
815 **1C, D**), it followed that:

816 $$N_{Tw(RwC)} \text{ (from } \textbf{Figure 1C}\text{)} = N_{(TwC)wR} \text{ (from } \textbf{Figure 1D}\text{)} \quad \text{(S2)}$$

817 Using the definitions of $p\big(Tw(RwC)\big)$, $p(TwR|TwC)$ and $p(TwC)$ (Eqs. 1, 6 and 8), it then
818 followed that:

819 $$p\big(Tw(RwC)\big) = N_{Tw(RwC)}/N_T = N_{(TwC)wR}/N_T = \big(N_{(TwC)wR}/N_{TwC}\big)(N_{TwC}/N_T)$$

820 $$= p(TwR|TwC)p(TwC) \quad \text{(S3)}$$

821 Using Eq. S3 in Eq. 10, the expected value of $p^{rs}\big(Tw(RwC)\big)$ could thus be calculated from the
822 input parameters as follows:

823 $$p^{rs}\big(Tw(RwC)\big) = p(TwR|TwC)p(TwC)/p(RwC) \quad \text{(S4)}$$

824 With similar arguments, the expected value of $p^{rs}\big(Tw(RnC)\big)$ was calculated from the input
825 parameters as follows:

826 $$p^{rs}\big(Tw(RnC)\big) = p(TwR|TnC)\big(1 - p(TwC)\big)/\big(1 - p(RwC)\big) \quad \text{(S5)}$$

827

828 ## Supplemental Material

829 There are three supplemental figures.

830

831 ## Acknowledgements

832 We thank Dr. Tieqiao Zhang for microscopy support, Dr. Anthony R. Vega for initial programming of code
833 for pairwise colocalization of punctate objects, and the Lavis lab (Janelia Research Campus, Ashburn, VA)
834 for JF549-Halo ligand. This work was supported by funding from NIH/NIGMS (R35 GM119619), the Welch

835 Foundation (I-1901) and the UT Southwestern Endowed Scholars Program to KJ, and the Canadian
836 Institutes of Health Research (CIHR PS 165816) and Natural Sciences and Engineering Research Council
837 (NSERC RGPIN-2018-05783) to NT. JVL was an honorary trainee of the NIH Molecular Biophysics Training
838 Grant (5T32GM131963; PI: Dr. Yuh Min Chook), and was also supported by a Diversity Supplement to NIH
839 grant R35 GM119619 (PI: KJ). The authors declare no competing financial interests.
840

841 ## Author contributions

842 KJ, JVL and BRA designed research; JVL and KJ developed algorithm; JVL wrote software; BRA and AD
843 performed experiments; JVL and BRA performed analysis; NT made HaloTag-CD36 plasmid; KJ, JVL and
844 BRA wrote paper with input from all co-authors.
845

846 ## References

847 Abedi, H., and I. Zachary. 1997. Vascular endothelial growth factor stimulates tyrosine phosphorylation
848 and recruitment to new focal adhesions of focal adhesion kinase and paxillin in endothelial cells.
849 *J Biol Chem*. 272:15442-15451.
850 Aguet, F., C.N. Antonescu, M. Mettlen, S.L. Schmid, and G. Danuser. 2013. Advances in analysis of low
851 signal-to-noise images link dynamin and AP2 to the functions of an endocytic checkpoint. *Dev Cell*.
852 26:279-291.
853 Bachmann, M., S. Kukkurainen, V.P. Hytönen, and B. Wehrle-Haller. 2019. Cell Adhesion by Integrins.
854 *Physiol Rev*. 99:1655-1699.
855 Basagiannis, D., S. Zografou, C. Murphy, T. Fotsis, L. Morbidelli, M. Ziche, C. Bleck, J. Mercer, and S.
856 Christoforidis. 2016. VEGF induces signalling and angiogenesis by directing VEGFR2 internalisation
857 through macropinocytosis. *J Cell Sci*. 129:4091-4104.
858 Bates, M., B. Huang, G.T. Dempsey, and X. Zhuang. 2007. Multicolor Super-Resolution Imaging with Photo-
859 Switchable Fluorescent Probes. *Science*. 317:1749-1753.
860 Birch, C.A., O. Molinar-Inglis, and J. Trejo. 2021. Subcellular hot spots of GPCR signaling promote vascular
861 inflammation. *Curr Opin Endocr Metab Res*. 16:37-42.
862 Birukova, A.A., I. Cokic, N. Moldobaeva, and K.G. Birukov. 2009. Paxillin is involved in the differential
863 regulation of endothelial barrier by HGF and VEGF. *Am J Respir Cell Mol Biol*. 40:99-107.
864 Bolte, S., and F.P. Cordelières. 2006. A guided tour into subcellular colocalization analysis in light
865 microscopy. *J Microsc*. 224:213-232.
866 Byron, A., J.D. Humphries, J.A. Askari, S.E. Craig, A.P. Mould, and M.J. Humphries. 2009. Anti-integrin
867 monoclonal antibodies. *J Cell Sci*. 122:4009-4011.
868 Caetano, F.A., B.S. Dirk, J.H.K. Tam, P.C. Cavanagh, M. Goiko, S.S.G. Ferguson, S.H. Pasternak, J.D.
869 Dikeakos, J.R. de Bruyn, and B. Heit. 2015. MIiSR: Molecular Interactions in Super-Resolution
870 Imaging Enables the Analysis of Protein Interactions, Dynamics and Formation of Multi-protein
871 Structures. *Plos Computational Biology*. 11.
872 Charrin, S., F. Le Naour, O. Silvie, P.E. Milhiet, C. Boucheix, and E. Rubinstein. 2009. Lateral organization
873 of membrane proteins: tetraspanins spin their web. *Biochem. J.* 420:133-154.

874 da Rocha-Azevedo, B., S. Lee, A. Dasgupta, A.R. Vega, L.R. de Oliveira, T. Kim, M. Kittisopikul, Z.A. Malik,
875 and K. Jaqaman. 2020. Heterogeneity in VEGF Receptor-2 Mobility and Organization on the
876 Endothelial Cell Surface Leads to Diverse Models of Activation by VEGF. *Cell Rep*. 32:108187.
877 Delos Santos, R.C., C. Garay, and C.N. Antonescu. 2015. Charming neighborhoods on the cell surface:
878 plasma membrane microdomains regulate receptor tyrosine kinase signaling. *Cell Signal*. 27:1963-
879 1976.
880 Diggle, P.J. 2014. Statistical Analysis of Spatial and Spatiotemporal Point Patterns. CRC Press, Boca Raton,
881 FL.
882 Dunn, K.W., M.M. Kamocka, and J.H. McDonald. 2011. A practical guide to evaluating colocalization in
883 biological microscopy. *Am J Physiol Cell Physiol*. 300:C723-742.
884 Eichmann, A., and M. Simons. 2012. VEGF signaling inside vascular endothelial cells and beyond. *Current*
885 *Opinion in Cell Biology*. 24:188-193.
886 Ferrara, N., H.P. Gerber, and J. LeCouter. 2003. The biology of VEGF and its receptors. *Nat Med*. 9:669-
887 676.
888 Fletcher, P.A., D.R.L. Scriven, M.N. Schulson, and E.D.W. Moore. 2010. Multi-Image Colocalization and Its
889 Statistical Significance. *Biophysical Journal*. 99:1996-2005.
890 Gammella, E., P. Buratti, G. Cairo, and S. Recalcati. 2017. The transferrin receptor: the cellular iron gate.
891 *Metallomics*. 9:1367-1375.
892 Geiger, B., J.P. Spatz, and A.D. Bershadsky. 2009. Environmental sensing through focal adhesions. *Nat Rev*
893 *Mol Cell Biol*. 10:21-33.
894 Gingras, A.C., K.T. Abe, and B. Raught. 2019. Getting to know the neighborhood: using proximity-
895 dependent biotinylation to characterize protein complexes and map organelles. *Current Opinion*
896 *in Chemical Biology*. 48:44-54.
897 Githaka, J.M., A.R. Vega, M.A. Baird, M.W. Davidson, K. Jaqaman, and N. Touret. 2016. Ligand-induced
898 growth and compaction of CD36 nanoclusters enriched in Fyn induces Fyn signaling. *J Cell Sci*.
899 129:4175-4189.
900 Gordon, E.J., D. Fukuhara, S. Weström, N. Padhan, E.O. Sjöström, L. van Meeteren, L. He, F. Orsenigo, E.
901 Dejana, K. Bentley, A. Spurkland, and L. Claesson-Welsh. 2016. The endothelial adaptor molecule
902 TSAd is required for VEGF-induced angiogenic sprouting through junctional c-Src activation. *Sci*
903 *Signal*. 9:ra72.
904 Heit, B., H. Kim, G. Cosio, D. Castano, R. Collins, C.A. Lowell, K.C. Kain, W.S. Trimble, and S. Grinstein. 2013.
905 Multimolecular Signaling Complexes Enable Syk-Mediated Signaling of CD36 Internalization. *Dev.*
906 *Cell*. 24:372-383.
907 Helmuth, J.A., G. Paul, and I.F. Sbalzarini. 2010. Beyond co-localization: inferring spatial interactions
908 between sub-cellular structures from microscopy images. *BMC Bioinformatics*. 11:372.
909 Huang, B., M. Bates, and X.W. Zhuang. 2009. Super-Resolution Fluorescence Microscopy. *Annual Review*
910 *of Biochemistry*. 78:993-1016.
911 Huang, W.X., M. Febbraio, and R.L. Silverstein. 2011. CD9 Tetraspanin Interacts with CD36 on the Surface
912 of Macrophages: A Possible Regulatory Influence on Uptake of Oxidized Low Density Lipoprotein.
913 *PLoS One*. 6.
914 Hynes, R.O. 2002. Integrins: bidirectional, allosteric signaling machines. *Cell*. 110:673-687.
915 Jaqaman, K., and J.A. Ditlev. 2021. Biomolecular condensates in membrane receptor signaling. *Curr Opin*
916 *Cell Biol*. 69:48-54.
917 Jaqaman, K., J.A. Galbraith, M.W. Davidson, and C.G. Galbraith. 2016. Changes in single-molecule integrin
918 dynamics linked to local cellular behavior. *Mol Biol Cell*. 27:1561-1569.
919 Jaqaman, K., D. Loerke, M. Mettlen, H. Kuwata, S. Grinstein, S.L. Schmid, and G. Danuser. 2008. Robust
920 single-particle tracking in live-cell time-lapse sequences. *Nat Methods*. 5:695-702.

921 Kazerounian, S., M. Duquette, M.A. Reyes, J.T. Lawler, K.L. Song, C. Perruzzi, L. Primo, R. Khosravi-Far, F.
922 Bussolino, I. Rabinovitz, and J. Lawler. 2011. Priming of the vascular endothelial growth factor
923 signaling pathway by thrombospondin-1, CD36, and spleen tyrosine kinase. *Blood*. 117:4658-
924 4666.
925 Kittisopikul, M., A. Vahabikashi, T. Shimi, R.D. Goldman, and K. Jaqaman. 2020. Adaptive multiorientation
926 resolution analysis of complex filamentous network images. *Bioinformatics*. 36:5093-5103.
927 Kleinschmidt, E.G., and D.D. Schlaepfer. 2017. Focal adhesion kinase signaling in unexpected places. *Curr*
928 *Opin Cell Biol*. 45:24-30.
929 Kwaaitaal, M., N.F. Keinath, S. Pajonk, C. Biskup, and R. Panstruga. 2010. Combined Bimolecular
930 Fluorescence Complementation and Forster Resonance Energy Transfer Reveals Ternary SNARE
931 Complex Formation in Living Plant Cells. *Plant Physiology*. 152:1135-1147.
932 Lachmanovich, E., D.E. Shvartsman, Y. Malka, C. Botvin, Y.I. Henis, and A.M. Weiss. 2003. Co-localization
933 analysis of complex formation among membrane proteins by computerized fluorescence
934 microscopy: application to immunofluorescence co-patching studies. *Journal of Microscopy*.
935 212:122-131.
936 Lagache, T., A. Grassart, S. Dallongeville, O. Faklaris, N. Sauvonnet, A. Dufour, L. Danglot, and J.C. Olivo-
937 Marin. 2018. Mapping molecular assemblies with fluorescence microscopy and object-based
938 spatial statistics. *Nature Communications*. 9.
939 Lagache, T., N. Sauvonnet, L. Danglot, and J.C. Olivo-Marin. 2015. Statistical analysis of molecule
940 colocalization in bioimaging. *Cytometry A*. 87:568-579.
941 Lampugnani, M.G., F. Orsenigo, M.C. Gagliani, C. Tacchetti, and E. Dejana. 2006. Vascular endothelial
942 cadherin controls VEGFR-2 internalization and signaling from intracellular compartments. *J Cell*
943 *Biol*. 174:593-604.
944 Lanahan, A.A., K. Hermans, F. Claes, J.S. Kerley-Hamilton, Z.W. Zhuang, F.J. Giordano, P. Carmeliet, and M.
945 Simons. 2010. VEGF receptor 2 endocytic trafficking regulates arterial morphogenesis. *Dev Cell*.
946 18:713-724.
947 Le Dévédec, S.E., B. Geverts, H. de Bont, K. Yan, F.J. Verbeek, A.B. Houtsmuller, and B. van de Water. 2012.
948 The residence time of focal adhesion kinase (FAK) and paxillin at focal adhesions in renal epithelial
949 cells is determined by adhesion size, strength and life cycle status. *Journal of Cell Science*.
950 125:4498-4506.
951 Linkert, M., C.T. Rueden, C. Allan, J.M. Burel, W. Moore, A. Patterson, B. Loranger, J. Moore, C. Neves, D.
952 MacDonald, A. Tarkowska, C. Sticco, E. Hill, M. Rossner, K.W. Eliceiri, and J.R. Swedlow. 2010.
953 Metadata matters: access to image data in the real world. *J. Cell Biol.* 189:777-782.
954 Liu, A.P., F. Aguet, G. Danuser, and S.L. Schmid. 2010. Local clustering of transferrin receptors promotes
955 clathrin-coated pit initiation. *J Cell Biol*. 191:1381-1393.
956 López-Colomé, A.M., I. Lee-Rivera, R. Benavides-Hidalgo, and E. López. 2017. Paxillin: a crossroad in
957 pathological cell migration. *J Hematol Oncol*. 10:50.
958 Lucas, A.M., P.V. Ryder, B. Li, B.A. Cimini, K.W. Eliceiri, and A.E. Carpenter. 2021. Open-source deep-
959 learning software for bioimage segmentation. *Mol Biol Cell*. 32:823-829.
960 Marlowe, T.A., F.L. Lenzo, S.A. Figel, A.T. Grapes, and W.G. Cance. 2016. Oncogenic Receptor Tyrosine
961 Kinases Directly Phosphorylate Focal Adhesion Kinase (FAK) as a Resistance Mechanism to FAK-
962 Kinase Inhibitors. *Mol Cancer Ther*. 15:3028-3039.
963 Mayle, K.M., A.M. Le, and D.T. Kamei. 2012. The intracellular trafficking pathway of transferrin. *Biochim*
964 *Biophys Acta*. 1820:264-281.
965 Miao, W.M., E. Vasile, W.S. Lane, and J. Lawler. 2001. CD36 associates with CD9 and integrins on human
966 blood platelets. *Blood*. 97:1689-1696.
967 Mitra, S.K., D.A. Hanson, and D.D. Schlaepfer. 2005. Focal adhesion kinase: in command and control of
968 cell motility. *Nat Rev Mol Cell Biol*. 6:56-68.

969 Murphy, J.M., K. Jeong, Y.A.R. Rodriguez, J.H. Kim, E.E. Ahn, and S.S. Lim. 2019. FAK and Pyk2 activity
970 promote TNF-α and IL-1β-mediated pro-inflammatory gene expression and vascular
971 inflammation. *Sci Rep*. 9:7617.
972 Pastorek, L., M. Sobol, and P. Hozak. 2016. Colocalization coefficients evaluating the distribution of
973 molecular targets in microscopy methods based on pointed patterns. *Histochemistry and Cell*
974 *Biology*. 146:391-406.
975 Power, R.M., and J. Huisken. 2017. A guide to light-sheet fluorescence microscopy for multiscale imaging.
976 *Nature Methods*. 14:360-373.
977 Primo, L., C. Ferrandi, C. Roca, S. Marchio, L. di Blasio, M. Alessio, and F. Bussolino. 2005. Identification of
978 CD36 molecular features required for its in vitro angiostatic activity. *Faseb J.* 19:1713-+.
979 Rigiracciolo, D.C., M.F. Santolla, R. Lappano, A. Vivacqua, F. Cirillo, G.R. Galli, M. Talia, L. Muglia, M.
980 Pellegrino, N. Nohata, M.T. Di Martino, and M. Maggiolini. 2019. Focal adhesion kinase (FAK)
981 activation by estrogens involves GPER in triple-negative breast cancer cells. *J Exp Clin Cancer Res*.
982 38:58.
983 Romei, M.G., and S.G. Boxer. 2019. Split Green Fluorescent Proteins: Scope, Limitations, and Outlook. *In*
984 Annual Review of Biophysics, Vol 48. Vol. 48. K.A. Dill, editor. 19-44.
985 Sahl, S.J., S.W. Hell, and S. Jakobs. 2017. Fluorescence nanoscopy in cell biology. *Nat. Rev. Mol. Cell Biol.*
986 18:685-701.
987 Sastre, D., I. Estadella, M. Bosch, and A. Felipe. 2019. Triple-Colocalization Approach to Assess Traffic
988 Patterns and Their Modulation. *In* Computer Optimized Microscopy. Vol. 2040. Humana Press,
989 New York, NY. 215-234.
990 Scott, B.L., and A.D. Hoppe. 2015. Optimizing fluorescent protein trios for 3-Way FRET imaging of protein
991 interactions in living cells. *Scientific Reports*. 5.
992 Sezgin, E., I. Levental, S. Mayor, and C. Eggeling. 2017. The mystery of membrane organization:
993 composition, regulation and roles of lipid rafts. *Nat. Rev. Mol. Cell Biol.* 18:361-374.
994 Silverstein, R.L., and M. Febbraio. 2009. CD36, a Scavenger Receptor Involved in Immunity, Metabolism,
995 Angiogenesis, and Behavior. *Sci. Signal.* 2.
996 Simons, M., E. Gordon, and L. Claesson-Welsh. 2016. Mechanisms and regulation of endothelial VEGF
997 receptor signalling. *Nat Rev Mol Cell Biol*. 17:611-625.
998 Sorkin, A., and M. von Zastrow. 2009. Endocytosis and signalling: intertwining molecular networks. *Nat.*
999 *Rev. Mol. Cell Biol.* 10:609-622.
1000 Stauffer, W., H.J. Sheng, and H.N. Lim. 2018. EzColocalization: An ImageJ plugin for visualizing and
1001 measuring colocalization in cells and organisms. *Scientific Reports*. 8.
1002 Sulzmaier, F.J., C. Jean, and D.D. Schlaepfer. 2014. FAK in cancer: mechanistic findings and clinical
1003 applications. *Nat Rev Cancer*. 14:598-610.
1004 Sun, Y.S., C. Rombola, V. Jyothikumar, and A. Periasamy. 2013. Forster resonance energy transfer
1005 microscopy and spectroscopy for localizing protein-protein interactions in living cells. *Cytometry*
1006 *Part A*. 83:780-793.
1007 Sun, Z., X. Li, S. Massena, S. Kutschera, N. Padhan, L. Gualandi, V. Sundvold-Gjerstad, K. Gustafsson, W.W.
1008 Choy, G. Zang, M. Quach, L. Jansson, M. Phillipson, M.R. Abid, A. Spurkland, and L. Claesson-
1009 Welsh. 2012. VEGFR2 induces c-Src signaling and vascular permeability in vivo via the adaptor
1010 protein TSAd. *J Exp Med*. 209:1363-1377.
1011 Sungkaworn, T., M.L. Jobin, K. Burnecki, A. Weron, M.J. Lohse, and D. Calebiro. 2017. Single-molecule
1012 imaging reveals receptor-G protein interactions at cell surface hot spots. *Nature*. 550:543-547.
1013 Thomann, D., D.R. Rines, P.K. Sorger, and G. Danuser. 2002. Automatic fluorescent tag detection in 3D
1014 with super-resolution: application to the analysis of chromosome movement. *J Microsc*. 208:49-
1015 64.

1016 Thorne, R.F., J.F. Marshall, D.R. Shafren, P.G. Gibson, I.R. Hart, and G.F. Burns. 2000. The integrins
1017 alpha(3)beta(1) and alpha(6)beta(1) physically and functionally associate with CD36 in human
1018 melanoma cells - Requirement for the extracellular domain of CD36. *J. Biol. Chem.* 275:35264-
1019 35275.
1020 Valm, A.M., S. Cohen, W.R. Legant, J. Melunis, U. Hershberg, E. Wait, A.R. Cohen, M.W. Davidson, E. Betzig,
1021 and J. Lippincott-Schwartz. 2017. Applying systems-level spectral imaging and analysis to reveal
1022 the organelle interactome. *Nature*. 546:162-+.
1023 Vicente-Manzanares, M., and A.R. Horwitz. 2011. Adhesion dynamics at a glance. *J Cell Sci*. 124:3923-
1024 3927.
1025 Wagner, A. 2000. Robustness against mutations in genetic networks of yeast. *Nature Genetics*. 24:355-
1026 361.
1027 Winograd-Katz, S.E., R. Fassler, B. Geiger, and K.R. Legate. 2014. The integrin adhesome: from genes and
1028 proteins to human disease. *Nat. Rev. Mol. Cell Biol.* 15:273-288.
1029 Wu, L.W., L.D. Mayo, J.D. Dunbar, K.M. Kessler, O.N. Ozes, R.S. Warren, and D.B. Donner. 2000. VRAP is
1030 an adaptor protein that binds KDR, a receptor for vascular endothelial cell growth factor. *J Biol*
1031 *Chem*. 275:6059-6062.
1032 Yanez-Mo, M., O. Barreiro, M. Gordon-Alonso, M. Sala-Valdes, and F. Sanchez-Madrid. 2009. Tetraspanin-
1033 enriched microdomains: a functional unit in cell plasma membranes. *Trends in Cell Biology*.
1034 19:434-446.
1035 Yauch, R.L., A.R. Kazarov, B. Desai, R.T. Lee, and M.E. Hemler. 2000. Direct extracellular contact between
1036 integrin alpha(3)beta(1) and TM4SF protein CD151. *J. Biol. Chem.* 275:9230-9238.
1037 Zhang, B., J. Zerubia, and J.C. Olivo-Marin. 2007. Gaussian approximations of fluorescence microscope
1038 point-spread function models. *Appl Opt*. 46:1819-1829.
1039 Zhang, F., J. Kotha, L.K. Jennings, and X.A. Zhang. 2009. Tetraspanins and vascular functions. *Cardiovasc.*
1040 *Res.* 83:7-15.
1041 Zhang, J.Z. 2012. Genetic Redundancies and Their Evolutionary Maintenance. *In* Evolutionary Systems
1042 Biology. Vol. 751. O.S. Soyer, editor. 279-300.

1043

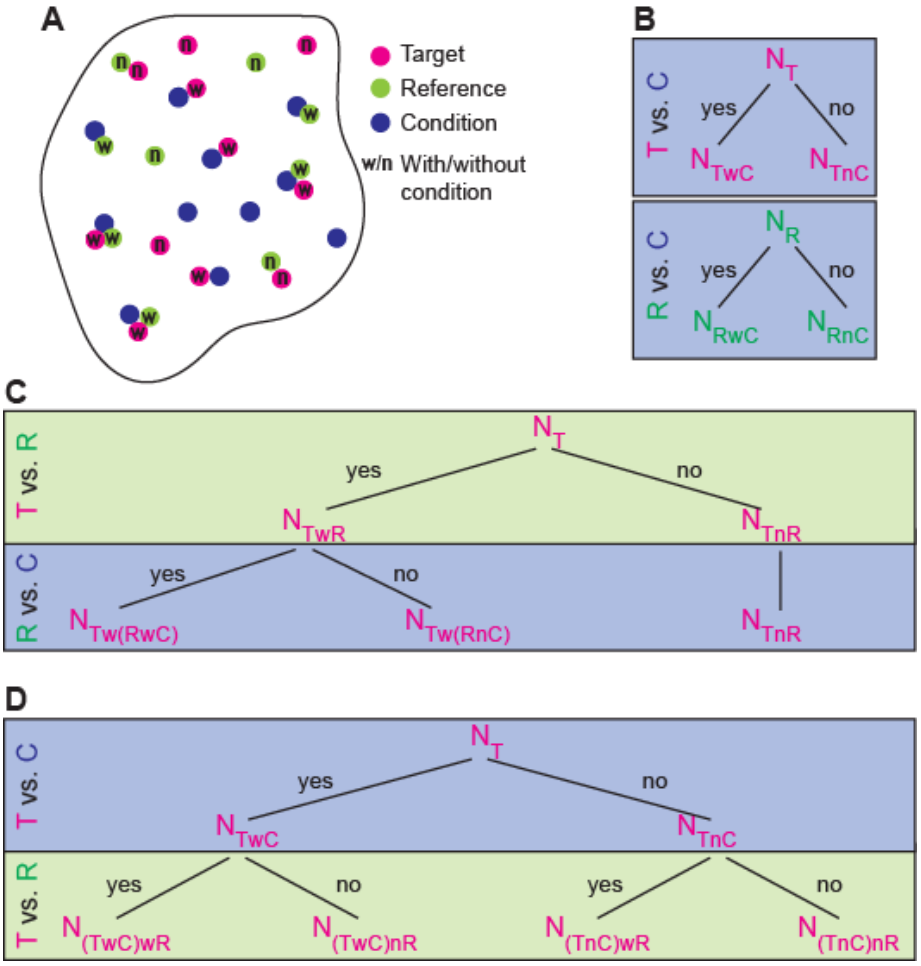

Figure 1. Schematic and decision trees for classifying target and reference objects in terms of their colocalization with condition objects and with each other. (A) Schematic of a "cell region" showing target (magenta) and reference (green) objects classified as with (w) or not with (n) condition objects (blue). **(B)** Decision trees for dividing target (top) and reference (bottom) objects into two groups each based on their colocalization ("yes" branch) or not ("no" branch) with condition objects. **(C)** Decision tree for first dividing target objects into colocalized or not with reference objects (top) and then, for target colocalized with reference, dividing them further based on reference colocalization with condition (bottom). **(D)** Decision tree for first dividing target objects into colocalized or not with condition (top) and then dividing each subgroup further based on target colocalization with reference.

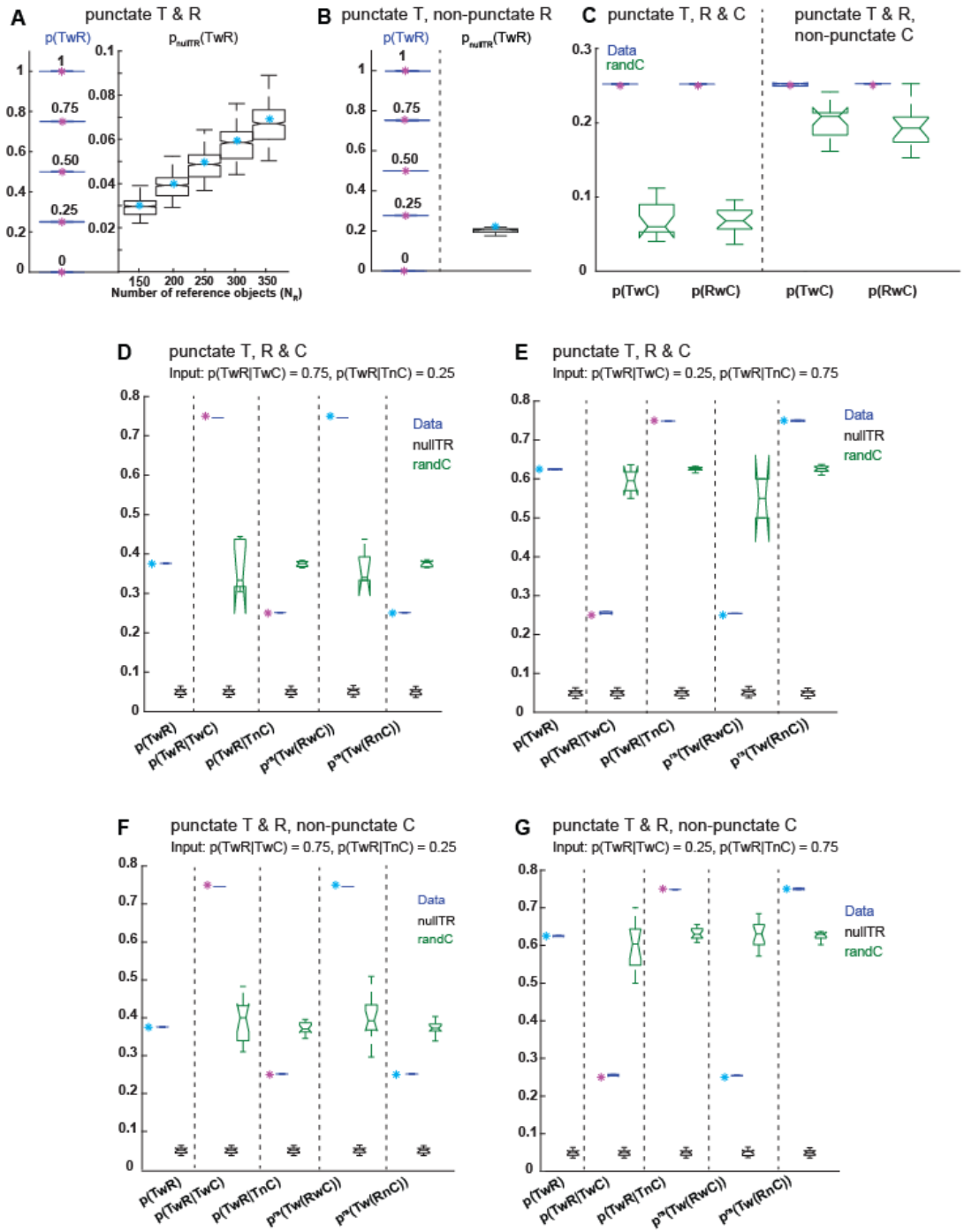

Figure 2. Analysis scheme accurately estimates conditional colocalization measures. (A, B) Calculated $p(TwR)$ (left) and corresponding $p_{nullTR}(TwR)$ (right) for simulations of punctate **(A)** and non-punctate **(B)** reference with punctate target. Each box shows the calculated values for all parameter combinations using the same input $p(TwR)$ or having the same expected $p_{nullTR}(TwR)$. Input/expected values are shown as magenta/cyan asterisks. For each box, the central mark is the median, the edges are the 25th and 75th percentiles, and the dashed whiskers extend to the most extreme data points. Notch around median indicates the 95% confidence interval of the median. In (A), each box represents N = 700 values (25 N_T and N_R combinations, or 25 N_T and $p(TwR)$ combinations, each repeated 28 times). In (B), each $p(TwR)$ box represents N = 140 values (5 N_T values, each repeated 28 times), while the $p_{nullTR}(TwR)$ box represents N = 700 values (25 N_T and $p(TwR)$ combinations, each repeated 28 times). **(C-G)** Representative results of calculated conditional colocalization measures. Each box represents N = 15 repeats of the stated simulation parameters. **(C)** Calculated $p(TwC)$ and $p(RwC)$ and their "randC" counterparts for simulations of punctate (left) and non-punctate (right) condition with punctate target and reference. Simulation parameters: $p(TwR|TwC)$=0.75, $p(TwR|TnC)$=0.25, $p(TwC)$=$p(RwC)$=0.25. Input values are shown as magenta asterisks. **(D-G)** Calculated conditional colocalization measures and their "nullTR" and "randC" counterparts for simulations of punctate **(D, E)** and non-punctate **(F, G)** condition with punctate target and reference, using the indicated $p(TwR|TwC)$ and $p(TwR|TnC)$ as well as $p(TwC)$=$p(RwC)$=0.25. Input/expected values are shown as magenta/cyan asterisks (see Materials and Methods for details).

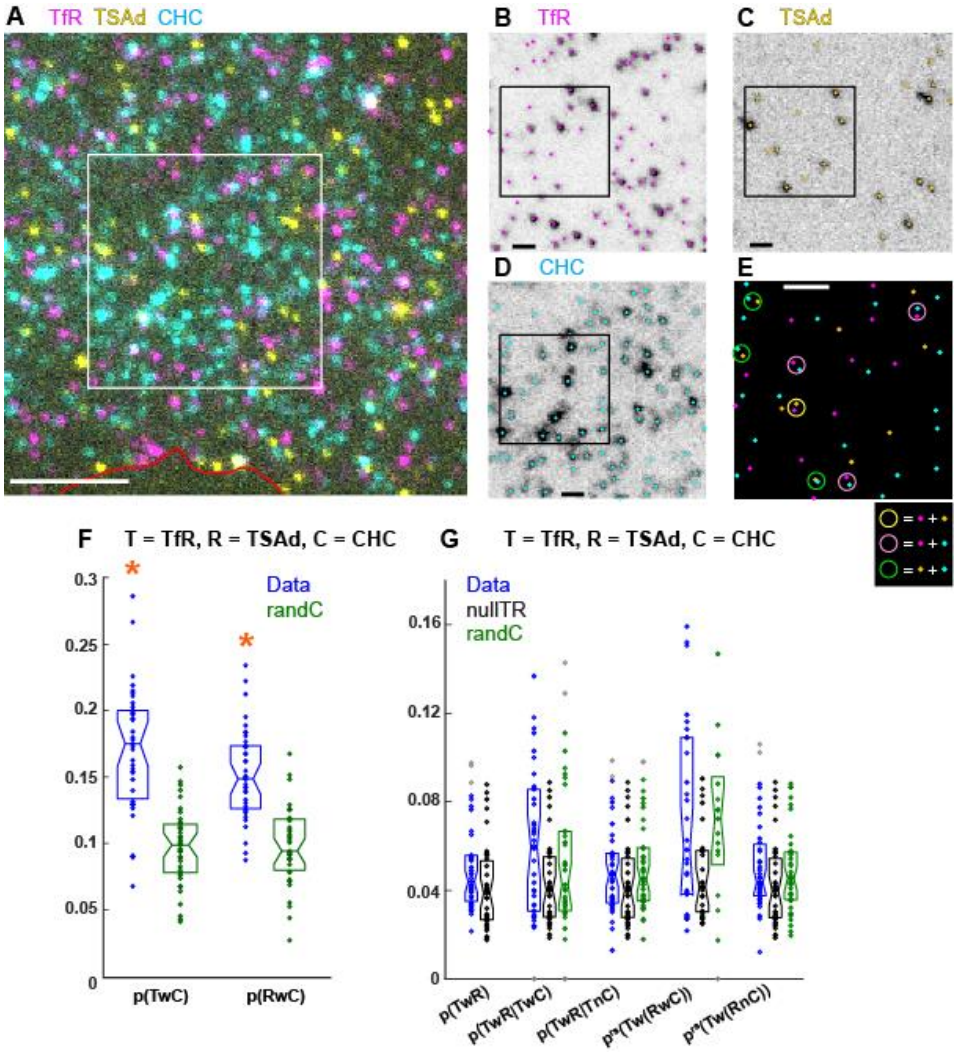

Figure 3: Conditional colocalization analysis correctly identifies no colocalization in an experimental negative control. (A) Representative three-color IF image of TfR, TSAd and CHC on the surface of a TIME cell imaged via TIRFM. Red line shows cell edge. Scale bar, 5 µm. **(B-D)** Particle detections (shown as dots) overlaid on the individual channels for the area within the white box in (A). Scale bar, 1 µm. **(E)** Overlay of the three channel detections for the area within the black box in (B-D), with color-coding following that in (B-D). Colored circles (diameter = 243 nm) point out colocalization events between the different molecules, following color-coding in legend. Scale bar, 1 µm. **(F)** Probabilities of target (TfR) and reference (TSAd) to colocalize with condition (CHC), together with their coincidental counterparts ("randC"). For each box, individual dots indicate individual cell measurements, the central mark is the median and the edges are the 25th and 75th percentiles. Notch around median indicates the 95% confidence interval of the median. Dots with same color as box are inliers and gray dots are outliers (as deemed by the Matlab "boxplot" function). Orange asterisks (*): $p < 0.01$, indicating that the probability of colocalization with condition is significantly greater than its coincidental counterpart, as assessed via a Wilcoxon rank-sum test. **(G)** Conditional colocalization measures and their coincidental counterparts ("nullTR" and "randC") for same object combination as in (F). Boxplots and dots as in (F). None of the conditional colocalization measures pass the significance test (See text), and thus none are highlighted. N = 39 cells from 4 repeats. See **Table 3** for number of objects per channel and other dataset properties.

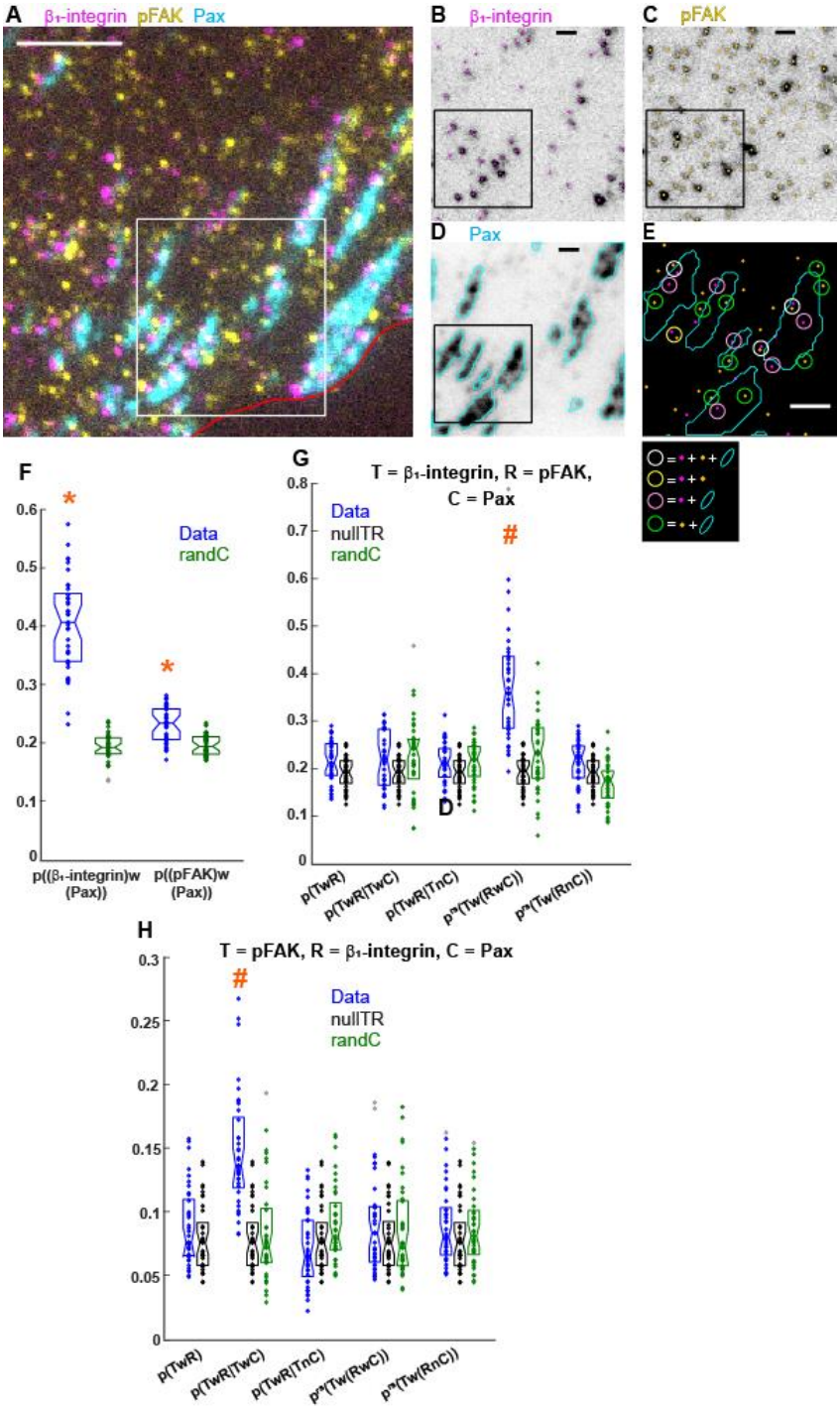

Figure 4: Conditional colocalization analysis captures the colocalization properties of an experimental positive control. (A) Representative three-color IF image of activated β1-integrin, pFAK and paxillin on the surface of a TIME cell imaged via TIRFM. Red line shows cell edge. Scale bar, 5 µm. **(B-D)** Particle detections (shown as dots in (B, C)) and patch segmentation (shown as outlines in (D)) overlaid on the individual channels for the area within the white box in (A). Scale bar, 1 µm. **(E)** Overlay of the three channel detections and segmentations for the area within the black box in (B-D), with color coding following that in (B-D). Colored circles (diameter = 243 nm) point out colocalization events between the different molecules, following color-coding in legend. Scale bar, 1 µm. **(F)** Probabilities of β1-integrin and pFAK to colocalize with the condition (paxillin; representing FAs), together with their coincidental counterparts ("randC"). Boxplots, dots and orange asterisks as in Figure 3F. **(G, H)** Conditional colocalization measures and their coincidental counterparts ("nullTR" and "randC") for target = β1-integrin and reference = pFAK **(G)** and vice versa **(H)**, both with condition = paxillin. Boxplots and dots as in Figure 3F. Orange pound signs (#): colocalization measure passes the significance test, i.e. it is significantly greater than its coincidental counterparts (both "nullTR" and "randC") and $p(TwR)$, as assessed via three Wilcoxon rank-sum tests. The significance threshold for each individual test is calculated using the Dunn–Sidak correction to give a total type-I error rate (for all three tests) of 0.05. N = 37 cells from 4 repeats. See **Table 3** for number of objects per channel and other dataset properties.

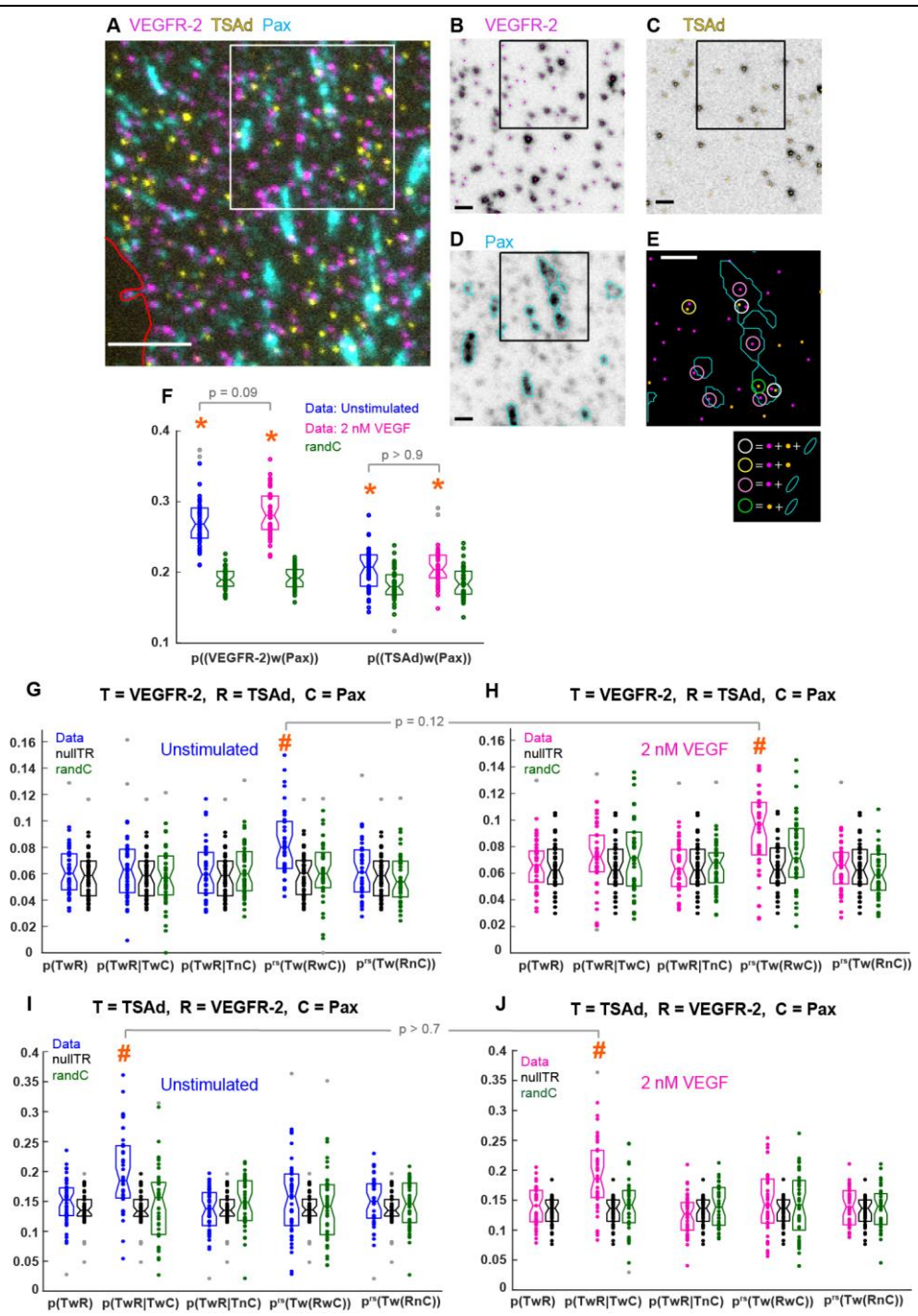

Figure 5: VEGFR-2-TSAd colocalization is enhanced for TSAd that is colocalized with FAs. **(A)** Representative three-color IF image of VEGFR-2, TSAd and paxillin on the surface of a TIME cell imaged via TIRFM. Red line shows cell edge. Scale bar, 5 µm. **(B-D)** Particle detections (shown as dots in (B, C)) and patch segmentation (shown as outlines in (D)) overlaid on the individual channels for the area within the black box in (A). Scale bar, 1 µm. **(E)** Overlay of the three channel detections and segmentations for the area within the black box in (B-D), with color coding following that in (B-D). Colored circles (diameter = 243 nm) point out the colocalization events between the different molecules, following color-coding in legend. Scale bar, 1 µm. **(F)** Probabilities of VEGFR-2 and TSAd to colocalize with the condition (paxillin; representing FAs), in the presence or absence of VEGF, together with their coincidental counterparts ("randC"). Boxplots, dots and orange asterisks as in Figure 3F. The probabilities in the absence and presence of VEGF were compared to each other using a Wilcoxon rank-sum test, resulting in indicated p-values. **(G-J)** Conditional colocalization measures and their coincidental counterparts ("nullTR" and "randC") for target = VEGFR-2 and reference = TSAd **(G, H)** and vice versa **(I, J)**, both with condition = paxillin, in the absence **(G, I)** or presence **(H, J)** of 2 nM VEGF. Boxplots, dots and orange pound signs as in Figure 4G. $p^{rs}(Tw(RwC)|TwC)$ and $p^{rs}(Tw(RnC)|TnC)$ were omitted because they did not provide useful information and, at the same time, they threw off the y-axis range (as observed for the negative and positive control analyses in Figures 3, 4). Significant measures were compared between the absence and presence of VEGF as in (F), yielding indicated p-values. N = 41 cells from 4 repeats. See **Table 3** for number of objects per channel and other dataset properties.

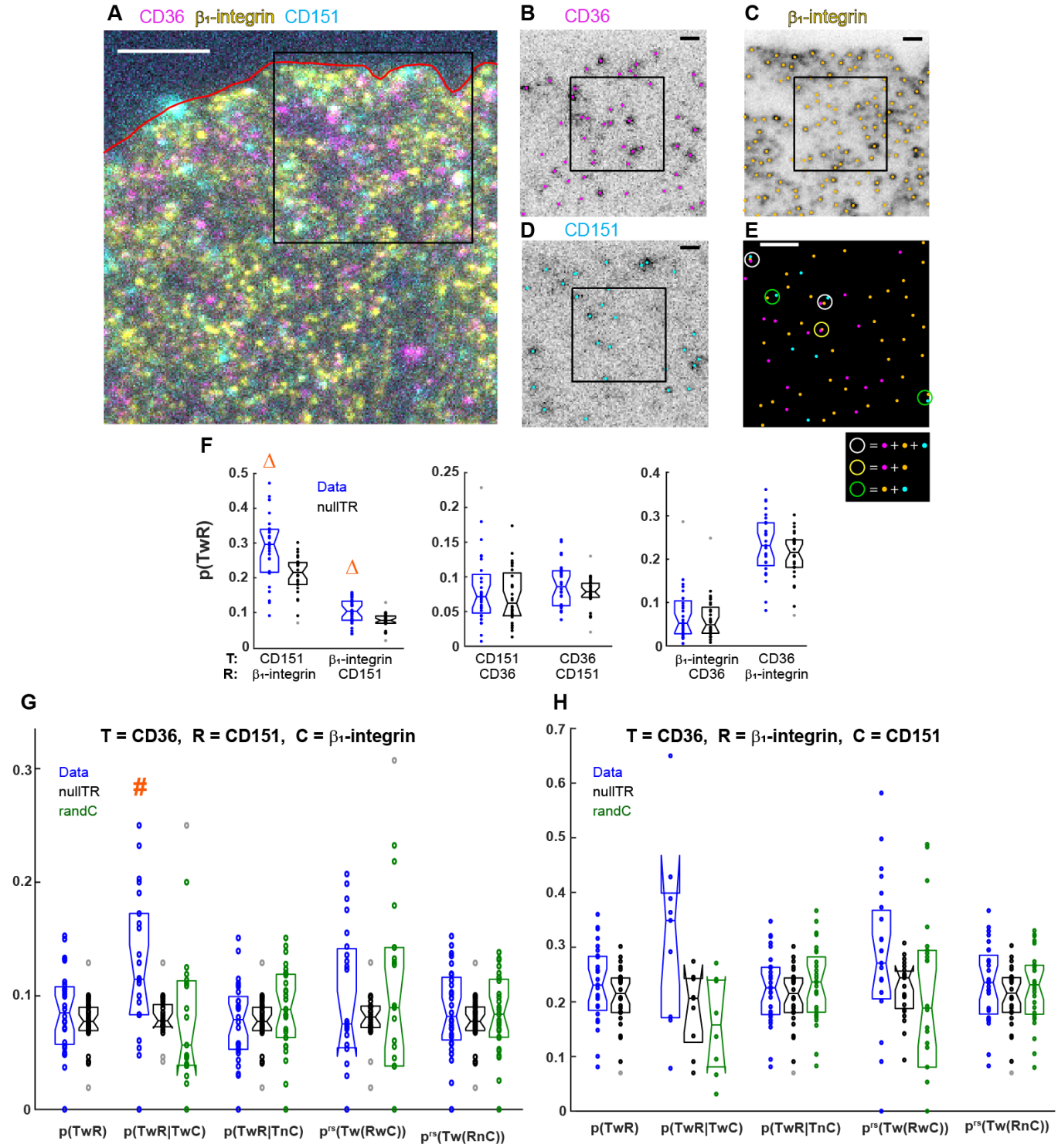

Figure 6: CD36 colocalizes with β1-integrin and CD151 together, with β1-integrin acting as the main mediator. (A) Representative three-color image of CD36, β1-integrin and CD151 on the surface of a TIME cell imaged via TIRFM. Red line shows cell edge. Scale bar, 5 µm. **(B-D)** Particle detections (shown as dots) overlaid on the individual channels for the area within the white box in (A). Scale bar, 1 µm. **(E)** Overlay of the three channel detections for the area within the black box in (B-D), with color-coding following that in (B-D). Colored circles (diameter = 267 nm) point out colocalization events between the different molecules, following color-coding in legend. Scale bar, 1 µm. **(F)** Overall probabilities of target to colocalize with reference ($p(TwR)$) for the different target and reference combinations among the imaged molecules, together with their coincidental counterparts ("nullTR"). Boxplots and dots as in Figure 3F. Orange triangles (Δ): $p < 0.01$, indicating that $p(TwR)$ is significantly greater than its coincidental counterpart, as assessed via a Wilcoxon rank-sum test. **(G, H)** Conditional colocalization measures and their coincidental counterparts ("nullTR" and "randC", as applicable) for indicated object combinations. Boxplots, dots and orange pound signs as in Figure 4G. $p^{rs}(Tw(RwC)|TwC)$ and $p^{rs}(Tw(RnC)|TnC)$ were omitted as in Figure 5G-J. N = 28 cells from 4 repeats. See **Table 3** for number of objects per channel and other dataset properties.

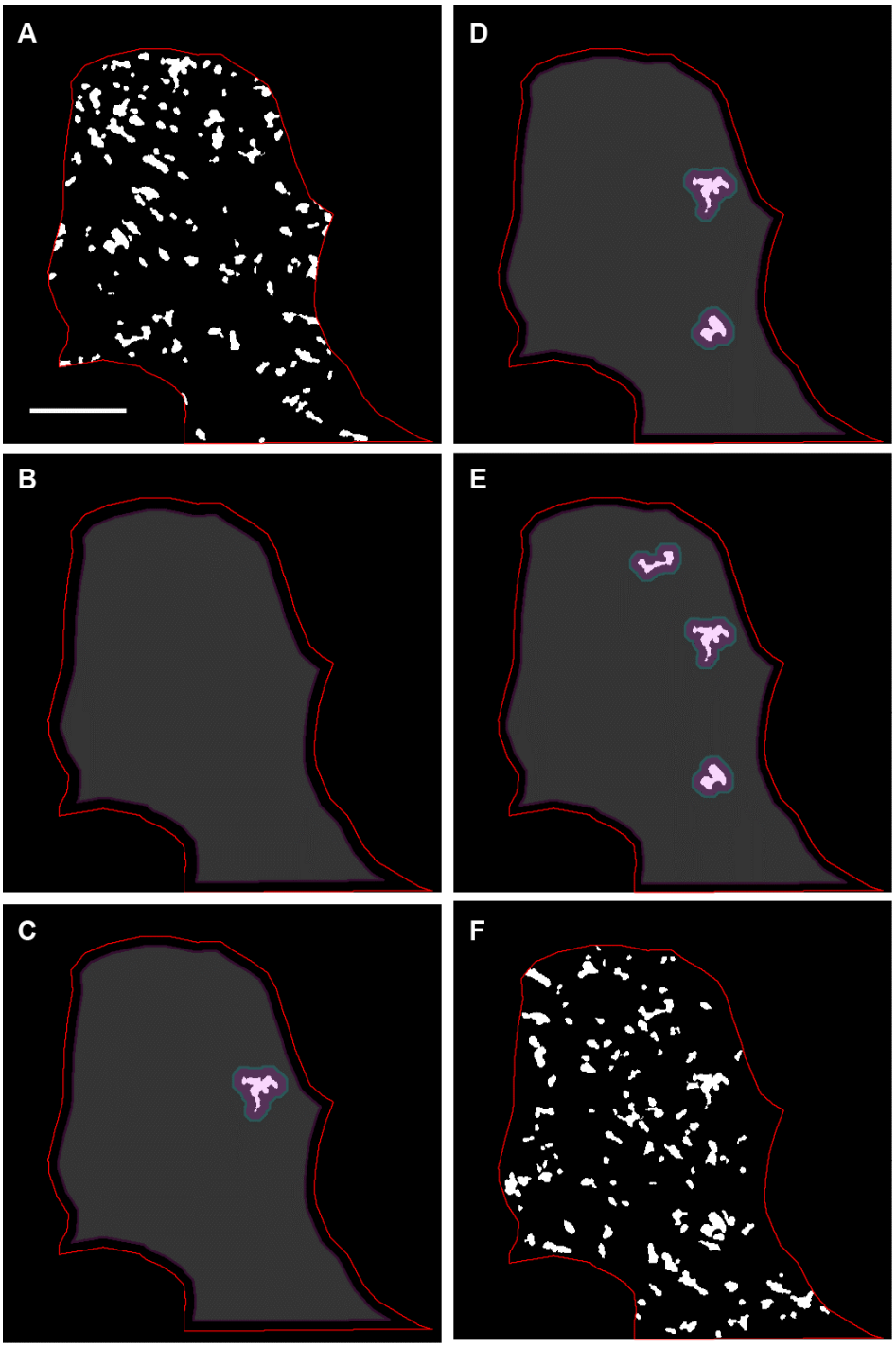

Suppl. Figure S1: Example illustrating randomization procedure for non-punctate condition objects. **(A)** Binary image of original paxillin patch segmentation. Red line outlines region of interest (ROI; the cell in the image in this case). Scale bar (applicable to all panels), 10 µm. **(B)** Available area for randomly placing the first condition object (gray-shaded area) within total ROI. **(C)** Random placement of first (largest) condition object, and the remaining available area (gray-shaded area), which excludes an area around the already placed object. **(D, E)** Random placement of second largest (D) and third largest (E) condition objects, and the remaining available area after each placement (gray-shaded area). **(F)** Final random placement of condition objects within the ROI.

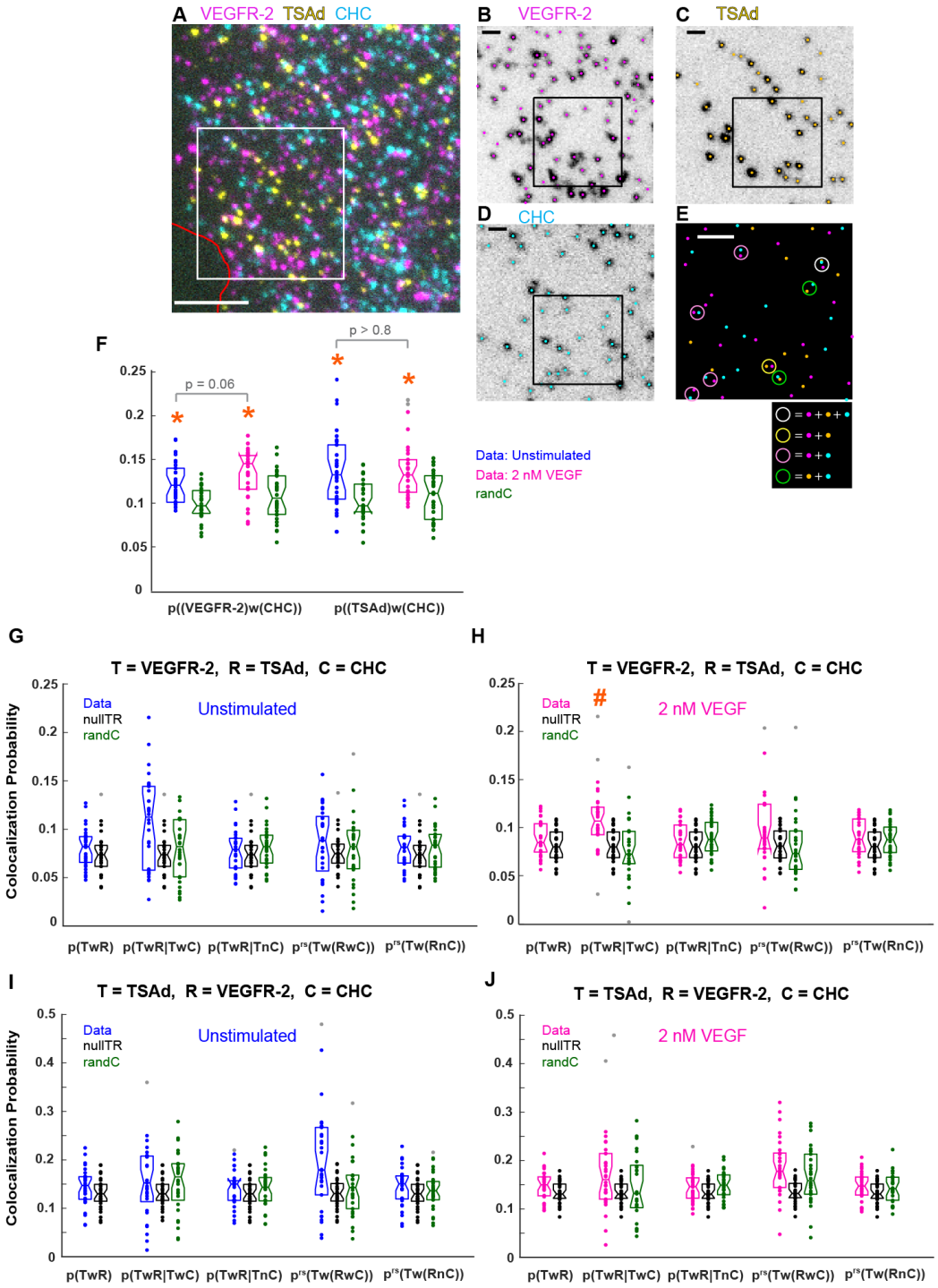

Suppl. Figure S2: VEGFR-2-TSAd colocalization is minimally influenced by their localization at CCSs. **(A)** Representative three-color IF image of VEGFR-2, TSAd and CHC on the surface of a TIME cell imaged via TIRFM. Red line shows cell edge. Scale bar, 5 µm. **(B-D)** Particle detections (shown as dots) overlaid on the individual channels for the area within the black box in (A). Scale bar, 1 µm. **(E)** Overlay of the three channel detections for the area within the black box in (B-D), with color coding following that in (B-D). Colored circles (diameter = 243 nm) point out the colocalization events between the different molecules, following color-coding in legend. Scale bar, 1 µm. **(F)** Probabilities of VEGFR-2 and TSAd to colocalize with the condition (CHC; representing CCSs), in the presence or absence of VEGF, together with their coincidental counterparts ("randC"). Boxplots, dots and orange asterisks as in Figure 3F. The probabilities in the absence and presence of VEGF were compared to each other using a Wilcoxon rank-sum test, resulting in indicated p-values. **(G-J)** Conditional colocalization measures and their coincidental counterparts ("nullTR" and "randC") for target = VEGFR-2 and reference = TSAd **(G, H)** and vice versa **(I, J)**, both with condition = CHC, in the absence **(G, I)** or presence **(H, J)** of 2 nM VEGF. Boxplots, dots and orange pound signs as in Figure 4G. $p^{rs}(Tw(RwC)|TwC)$ and $p^{rs}(Tw(RnC)|TnC)$ were omitted as in Figure 5G-H. As no measure was significant in both the absence and presence of VEGF, no statistical tests were performed to compare the two. N = 30 cells from 3 repeats. See **Table 3** for number of objects per channel and other dataset properties.

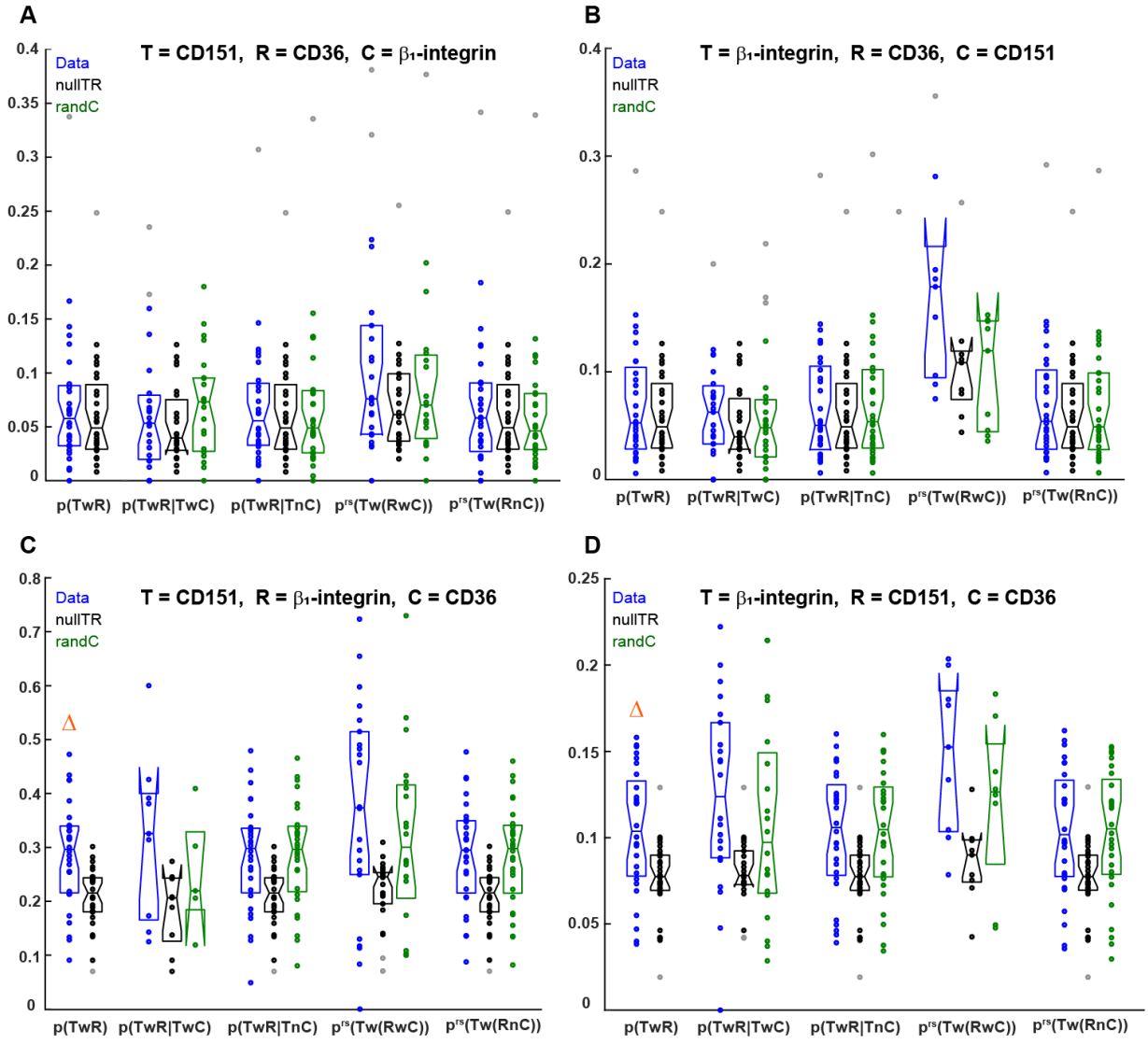

Suppl. Figure S3: Conditional colocalization analysis of CD36, β1-integrin and CD151 for the target, reference and condition permutations not shown in Figure 6. (A-D) Conditional colocalization measures and their coincidental counterparts ("nullTR" and "randC") for the following target, reference and condition combinations: **(A)** Target = CD151, reference = CD36 and condition = β1-integrin (target and reference switched relative to Figure 6G). **(B)** Target = β1-integrin, reference = CD36 and condition = CD151 (target and reference switched relative to Figure 6H). **(C)** Target = CD151, reference = β1-integrin and condition = CD36. (**D)** Target = β1-integrin, reference = CD151 and condition = CD36 (target and reference switched relative to (C)). Boxplots, dots and orange triangles as in Figure 6F. Other than $p(TwR)$ in (C) and (D), none of the conditional colocalization measures pass the significance test, and thus none are highlighted. N as in Figure 6. See **Table 3** for number of objects per channel and other dataset properties.